



## European volcanological supersite in Iceland: a monitoring system and network for the future

### Report

#### D7.3 - Tephra detector, infrasound and camera

Work Package:	<i>Determination and evolution of eruption source parameters</i>		
Work Package number:	7		
Deliverable:	<i>Tephra detector, infrasound and camera</i>		
Deliverable number:	7.3		
Type of Activity:	RTD		
Responsible activity leader:	<i>Magnus Tumi Gudmundsson</i>		
Responsible participant:	ITEM		
Authors:	<i>Emanuele Marchetti (ITEM), Maurizio Ripepe, (UNIFI), Thomas Walter (GFZ)</i>		

Type of Deliverable:	<i>Report</i>	<input checked="" type="checkbox"/>	<i>Demonstrator</i>	<input type="checkbox"/>
	<i>Prototype</i>	<input type="checkbox"/>	<i>Other</i>	<input type="checkbox"/>
Dissemination level:	<i>Public</i>	<input checked="" type="checkbox"/>	<i>Restricted Designated Group</i>	<input type="checkbox"/>
	<i>Prog. Participants (FP7)</i>	<input type="checkbox"/>	<i>Confidential (consortium)</i>	<input type="checkbox"/>



## Index

Abstract .....	2
1. Introduction .....	2
2. AshSizer, an instrument for real-time analysis of tephra fall-out .....	4
2.1 Instrument Design .....	4
2.1.1. The Optical Barrier .....	6
2.1.2. The Collector Unit .....	7
2.2. Central Unit .....	8
2.2.1. Overview .....	9
2.2.2. Acquisition Board .....	10
2.2.3. The Processing Board .....	14
2.2.4. Development of the first Central Unit prototype .....	16
2.3. AshSizer Calibration .....	17
2.3.1. Calibration of the Optical Barrier .....	18
2.3.2. Calibration of the Collector Unit .....	21
2.4. AshSizer client .....	23
2.4.1. Web Console .....	23
2.4.2. Output Data Format .....	24
2.4.3. AshViewer .....	26
2.5. Future steps in the AshSizer development .....	27
3. The FUTUREVOLC infrasound arrays .....	30
3.1. Instrumentation and deployment of FUTUREVOLC arrays .....	30
3.1.1. ICE 1 Array .....	31
3.1.2. ICE 2 Array .....	32
3.1.3. ICE 3 Array .....	32
3.2. Real-time infrasound array Processing .....	33
3.3. Results from the FUTUREVOLC Infrasound array network .....	34
3.3.1. The Bardabunga Seismic sequence .....	34
3.3.2. Landslide at Askja volcano .....	35
4. Algorithm for stereoscopic viewing field of 3D particle trajectories .....	37
5. References .....	40

## Abstract

The mass eruption rate (MER) is a critical information to be derived in order to estimate the size of a volcanic eruption and its effect in terms of ash dispersal. Within the FUTUREVOLC project, new techniques are developed to address this issue.

In particular, infrasound arrays are deployed to identify ongoing volcanic eruptions and to evaluate, following the preliminary results obtained during the 2010 eruption of volcano Eyjafjallajokull, the mass eruption rate by converting recorded infrasonic pressure to exit velocity and eventually to MER. 3 Infrasound arrays have been installed in Iceland within FUTUREVOLC project and real-time data are currently available.

Moreover, fixed streaming and time lapsed cameras are being installed on selected volcanoes and images analyzed with a photogrammetric approach. Image correlation techniques are being implemented to infer source parameters, such as precise vent location, vent motion and exit velocities.

Once the MER is known, in order to robustly assess the volcanic atmospheric ash dispersal, information of the total grain size distribution (GSD) of erupted material would be required. Such information is however not available until fall-out material is collected, analyzed in the laboratory and total GSD is eventually estimated. This analysis generally requires a long time (hours-days), thus making it useless for real-time operational purposes. For this reason, a new sensor for real-time automatic analysis of grain size distribution of fall out material (*AshSizer*) is being developed within the project, that providing GSD analysis in different sites in real-time might be used to infer the total GSD of erupted material. The prototype delivered already within the project allows real-time analysis of GSD of fall out material down to grain size of 100  $\mu\text{m}$  and provides information of the accumulation rate.

The present report summarizes the results obtained during the first 2 years of the FUTUREVOLC project for the installation of the infrasound arrays and camera expected in Task 7.1 and implementation of dedicated software and systems for the real-time evaluation of eruption source parameters. The development of the new sensor for real-time tephra fall-out analysis is presented in detail, as well as its functionality, remote control and initial calibration performed in the laboratory.

## 1. Introduction

The main aim of the WP7 of the FUTUREVOLC project is the determination and evolution of eruption source parameters, which are typically unknown for most eruptions worldwide while strongly affecting the resulting scenario. In order to robustly assess the ash dispersal concentration in the atmosphere, the eruption source parameters, and in particular the Mass Eruption Rate (MER), are essential information to be gathered. This is why the FUTUREVOLC project aims at developing new techniques and instruments that might provide critical information for modeling and risk assessment.

Volcanoes are efficient sources of infrasound. The near-field (<10 km) reduced atmospheric attenuation allows inferring source dynamics from infrasonic waveforms [e.g. Vergnolle and Brandeis, 1994] and the precise (<100 m) source location [e.g. Ripepe and Marchetti, 2002], whereas the efficient long range (3000-5000 km) propagation allows recording and monitoring far-field volcanic eruptions using large infrasonic arrays [e.g. Matoza et al., 2011]. These

features have been making infrasound observations on volcanoes more and more common, and infrasound monitoring of active volcanoes is now widely applied all around the world [see Johnson and Ripepe, 2011 for a review].

At short source-to-receiver distances (< 10s km), infrasound can provide important information for the assessment of ash dispersal in the atmosphere. During operational ash-cloud forecasting, prediction of ash concentration and total erupted mass directly depends on the determination of mass eruption rate (MER), which is typically inferred from plume height. Uncertainties for plume heights are large, especially for bent-over plumes in which the ascent dynamics are strongly affected by the surrounding wind field. Uncertainties can be reduced if MER is derived directly from geophysical observations of source dynamics. Ripepe et al. [2013] showed that acoustically derived MER can be converted into plume heights using field-based relationships and a 1D radially averaged buoyant plume theory model using a reconstructed total grain size distribution.

Within the FUTUREVOLC project 3 infrasound arrays are being deployed in Iceland, adding to a fourth system operating permanently since May 2010, in order to monitor volcanic eruptions in the country and estimate, even at large source-to-receiver distances (30-80 km), the mass eruption rate.

Visual observations of volcanoes provide amongst the strongest and most widely used information of eruption occurrence, plume height or other unrest changes (e.g. Walter, 2011). Within the FUTUREVOLC project fixed streaming and time lapsed cameras are being installed on selected volcanoes and images analyzed with a photogrammetric approach. Image correlation techniques are being implemented to infer source parameters, such as precise vent location, vent motion and exit velocities.

Following a volcanic eruption, the resulting ash dispersion in the atmosphere depends on atmospheric specification and on the characteristics of suspended volcanic ash. While to some extent atmospheric specifications are very well known, like for example the atmospheric models provided by European Center for Medium-range Weather Forecasts (ECMWF), the characteristics of suspended ash is generally unknown and assumptions are to be done. However, tests carried out on the Hekla 2000 eruption showed that the total grain size distribution (GSD) can be compiled by integrating measurements of GSD of fallout material performed along the dispersal axis (Bonadonna et al., 2009). However, such measurements are commonly performed after an event occurred, as they require the sampling of the material and its mechanical sieving thus preventing the use of this information for real-time assessment of ash dispersal in the atmosphere.

A new sensor is thus expected to be developed in the framework of the FUTUREVOLC project. Its main aim is to solve this issue, by providing an analysis of GSD of fallout material in near-real time, thus allowing the estimate of the total GSD of erupted material necessary for a more robust modeling of ash dispersal in the atmosphere.

The present report summarizes the results obtained during the first 2 years of the project for the installation and processing development for infrasound arrays and camera and about the development of the real-time tephra fall-out analyzer and its laboratory calibration.

## 2. AshSizer, an instrument for real-time analysis of tephra fall-out

The modelling of atmospheric ash dispersal is strongly controlled by the grain size distribution of erupted material, with fine ash transported far away in the plume and larger grain tephra deposited at closer distance from the vent. As a consequence, information of grain sizes is required, if a more reliable estimation of ash concentration in the atmosphere wants to be obtained. Here, the grain size of suspended ash might be inferred from the grain size distribution of fallout material, deposited at various distance from the eruptive vent.

In the framework of the FP7 EU project (FUTUREVOLC), a field instrument for real-time automatic measurement of grain-size–distribution of fallout material (AshSizer) is currently being developed, by Item s.r.l., a SME based in Italy working in the design and development of instruments for earth sciences and geophysics. The sensor development is performed in collaboration with University of Geneva, University of Iceland and University of Firenze. The main idea behind this work is to allow evaluating remotely and in near real-time the main properties of fallout material, in order to provide ground based constraints on the grain size distribution (GSD) of the suspended ash. This is primary information that is currently missing, necessary to optimize the dispersion models of volcanic ash.

A critical requirement that was considered while developing the sensor is connectivity as the AshSizer is likely to be developed in remote areas, where data transfer is strongly limited. Accordingly, the on-board electronics, processing and sensors, were chosen to allow limited power requirements and to provide on-board data processing and storage in order to optimize the data transfer efficiency.

The AshSizer was designed to operate in hostile environments, to perform the real-time analysis of grain size distribution and terminal velocity of tephra fallout particles as well as its accumulation rate (kg/s and m<sup>3</sup>/s) and to allow remote access to processed information as well as a limited amount of raw data. Here data transfer is minimal and optimize for low rate data transfer connections.

This report describes the design and development of the AshSizer performed by Item s.r.l. during the first 24 months of the project (first reporting period), when the prototype was delivered (Milestone 65 month 18) and eventually presented officially during the second FUTUREVOLC annual meeting. The report thus describes a state of the art of the AshSizer prototype, while additional testing is performed, mostly focusing on calibration and optimization of sensor connectivity, before the instruments will be developed in Iceland by month 30 of the project.

Following requirements and suggestions of some project partners interested in the topic, the instrument design has been slightly changed from what originally proposed, by adding a tephra collector and sensors for real-time measure of the weight and height of collected material, in addition to the optical barrier developed to evaluate real-time grain size distribution and fall out rate.

### 2.1 Instrument Design

In order to fulfil the expected requirements, and to satisfy the processing and data transfer limitations, it was chosen to measure the fall out material by laser obscuration, to couple that

with the collection of fall out material in a removable collector used to evaluate the accumulation rate (Figure 1) and to process all this information remotely on-board.

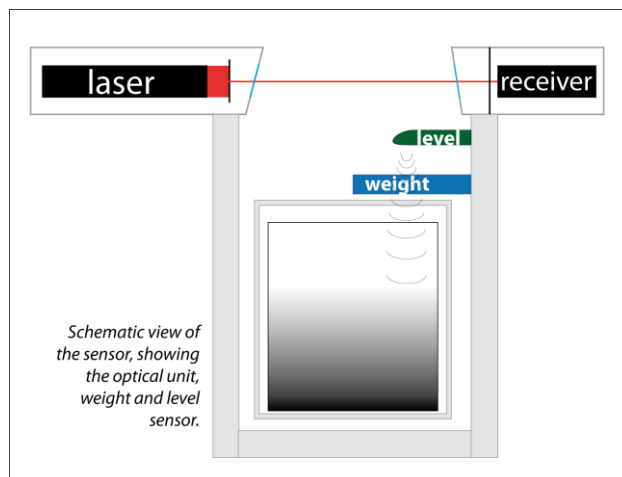


Figure 1: Schematic view (front view) of the AshSizer, designed to provide a real-time analysis of grain-size-distribution and accumulation rate of volcanic fallout as presented during the first project meeting in September 2013.

During the first year of work, the original idea of having a single sensor coupling both the optical barrier and the collector (Figure 1) was abandoned. The AshSizer prototype, completed by months 18 and presented officially on September 2014 during the second annual meeting of the project, is indeed composed on two main units, the optical barrier (70x10x50 cm, Optical Barrier) and the collector/electronic unit (30x30x60 cm, Collector Unit), which are connected to each other with a 5 m long cable. This allows an easier transportation and installation of the instrument as well as flexibility in sensor operation (Figure 2).

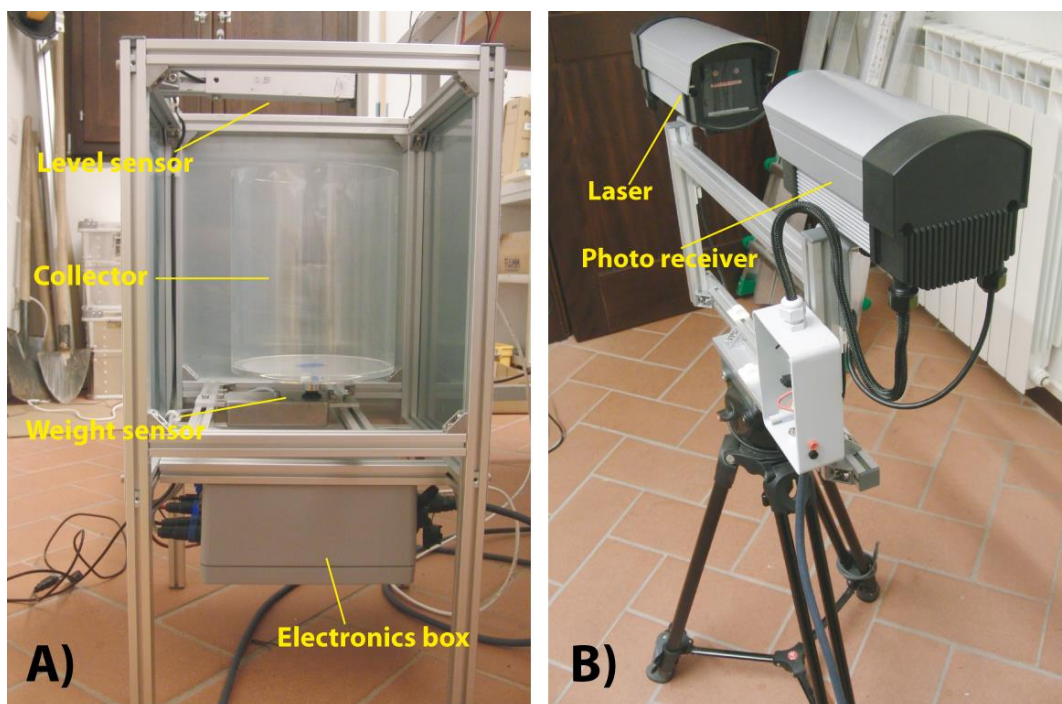


Figure 2: Picture of the Collector Unit (A) and Optical Barrier (B) of the AshSizer prototype, presented during the second annual meeting of the FUTUREVOLC project.

### 2.1.1. The Optical Barrier

The optical barrier, consists basically into a linear laser beam that is temporary obscured by the falling ash particles. The laser (wavelength 635 nm; red) emits a linear beam and is detected by a single photodiode, after beam focalization and wavelength filtering. The photodiode output is reflecting the integrated laser energy, and is thus affected by falling particles crossing the beam that are detected by decay in the analogue output of the photodiode. The laser obscuration is used to measure both the dimension and the vertical velocity of the particles crossing the laser beam. The first is basically resulting from the amplitude of laser obscuration, that is proportional to the cross section of the particles crossing the beam, while the second derives from the duration of the absorption signal (Figure 3).

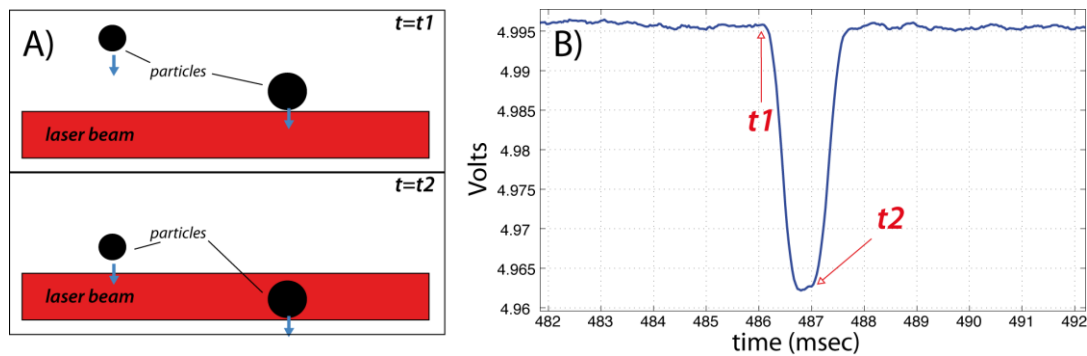


Figure 3: Schematic view (lateral view) of a single particles crossing the laser beam (A) and corresponding amplitude decay of the analogue output of the photodiode (B). The time stamps  $t1$  and  $t2$  corresponds to the time when the particle start entering and exiting the beam respectively.

The Optical Barrier is characterized by two main sections, the laser source section and the photo-receiver section (Figure 2, Figure 4). The laser source section is composed by a collimated laser source and a window of 1.6x30 mm that allows the laser beam to irradiate into the free-air as a linear laser beam (Figure 4). We chose a Schafer & Kirchoff (90CM-M140) laser with a wavelength of  $635 \pm 5$  nm (red). This model, despite being quite expensive, was chosen for the good quality of the laser optics that allows the beam to be extremely uniform over its entire cross-section. This is critical to ensure the same light absorption for a given particle for any position of the linear laser beam. The on-board electronics allow the laser to be switched on and off. The output power is adjustable through a potentiometer (1-100 %). Laser wavelength is  $635 \pm 5$  nm, while the laser power of collimated beam is of 2.2 mW. The optical maximum beam aperture is 37 mm, and the beam divergence is 0.012 mrad. Collimator housing is  $\varnothing$  45/49 mm. The instrument can be modulated by external analog or TTL source at a frequency up to 100 kHz. The operation temperature is up to 40 °C.

The photo-receiver section is composed by an optical section, a photo-detector and a signal amplifier. The optical section consists into a filter (636 nm, 10 nm bandwidth), that allows to minimise ambient noise, and a lens (40 mm diameter, 60 mm FL), which focuses the laser beam onto the photo-detector optical input, converting light intensity into electrical signal, that is in turn amplified in the 0-5 voltage range. The photo-detector is a PIN-3CD (Metal Package – D series) model and is characterized by a capacitance of 12pF and a dark current of 0.15-2 nA. In the prototype, the laser and the photo-receiver sections are protected using aluminium cases commonly employed for cameras.

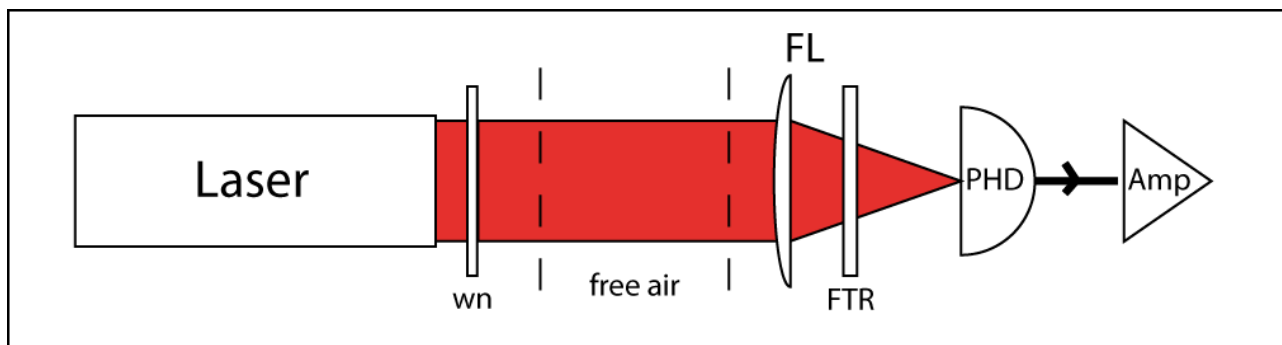


Figure 4: Schematic view of the Optical Barrier geometry, showing the laser, the window used to transform the cylindrical beam into linear (wn), the filter (FTR), focal lens (FL), the photodetector (PHD) and the amplifier (Amp).

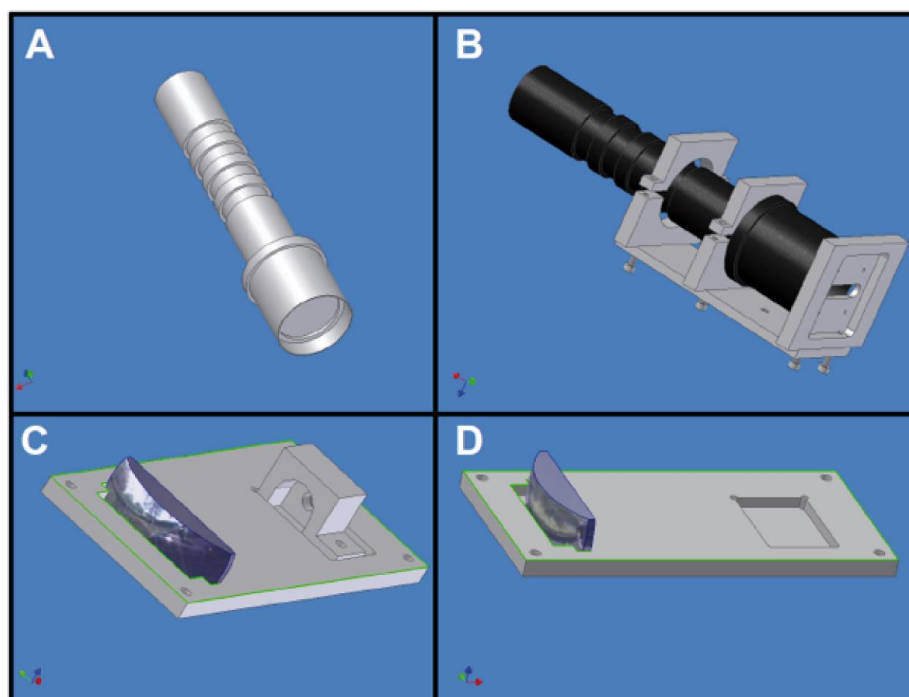


Figure 5: Computer-Aided Drafting (CAD) of the laser case (a), fixed mounting and windowing (b). (c, d) CAD project of the receiver optical section with fixed mounting for the photo-detector and the lens.

### 2.1.2. The Collector Unit

The collector unit of the AshSizer sensor, was developed following the requests advanced during the first year of the project, that in addition to measuring the GSD and the terminal velocity it would be fruitful to sample tephra fall-out in a dedicated collector and to measure in real-time the weight and level of the material inside the collector itself. Accordingly, a Collector Unit was designed and developed as a stand-alone structure, separated by the Optical Barrier, and equipped with a removable ash collector, weight and level sensors and an aluminium box which contains all the RT-Thepra electronics (Central Unit Figure 2a).

The collector is a PVC cylindrical collector (20 cm diameter, 22 cm high) that is positioned inside the central element for fall-out sampling above a weight sensor. The collector is fixed to an aluminium base through magnets that allow easy removal from the upper part of the central unit whenever required. A central hole allows aligning the collector on its base and water

drainage through a dedicated drainage system developed in the collector aluminium base (Figure 6).

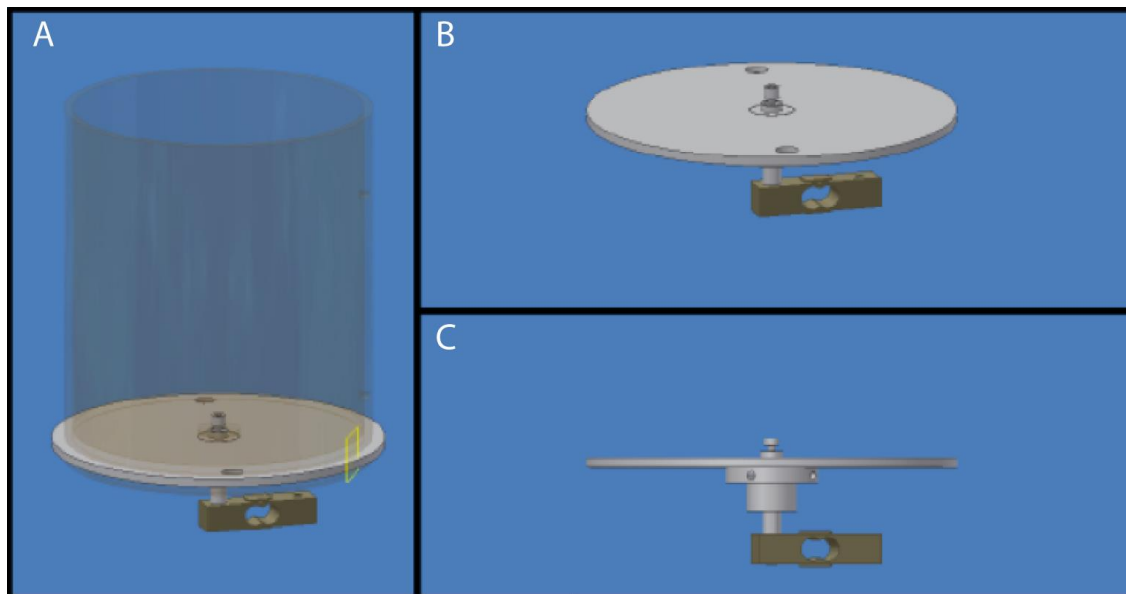


Figure 6: CAD project for ash collector (A), for the collector aluminium base (light grey) showing the load cell (dark grey) and drainage system (B, C).

A load cell (CZL635, 0-5 kg, 1 g resolution) is used to retrieve the collected ash weight. Its operation principle is based on the use of four strain gauge arranged in a Wheatstone bridge manner (Figure 6). In order to improve the overall system reliability an analog-to-digital converter has been integrated in the load cell sensor housing in order to provide a digital communication channel to the sensor electronics.

In addition to the weight, the level of the ash inside the collector is measured with an ultrasound sensor (SRF235), measuring the two-way distance from the sensor to a reflecting surface in the 10-120 cm range. Operating at 235 KHz and with a reflection with a beam of 15°, it is strongly range limited but ensures a resolution of ~ 1 mm.

At the base of the Collector Unit, an aluminium box holds all the sensor electronics and the sensor control unit (Central Unit). Here, raw data from the different sensors of the instrument are acquired and processed in real-time with an on-board microcomputer. Also the access and control of the instrument is performed through this unit.

## 2.2. Central Unit

The main features of the Central Unit are briefly described in this section. Its design and development started since the very beginning of the projet and was adapted to the requirements and requests advanced during the first year of the project. At the time of writing this report, the sensor electronics and control currently installed in the RT-Thepra prototype, have been tested extensively in the laboratory of Item s.r.l. and showed to be quite robust and efficient.

### 2.2.1. Overview

Figure 7 shows the overview of the Central Unit of the AshSizer sensor. Its main scope is to gather raw data from the sensors (Optical barrier, level and weight sensors), process data on-board in real-time and allow remote access to processing results. A brief description of the sensors is provided in the previous section of the present report.

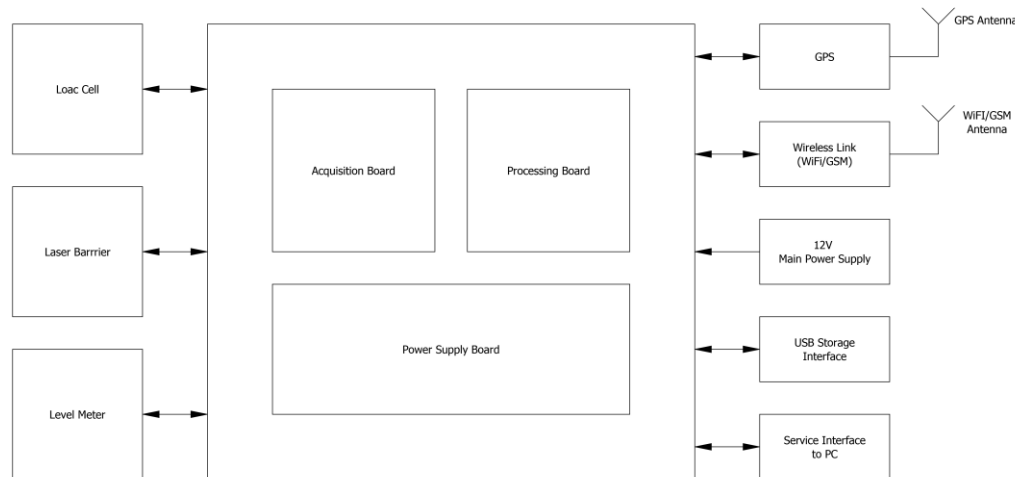


Figure 7: Overview of the Central Unit of the AshSizer sensor, showing the 3 main boards, additional subsystems and link to the sensors.

Within the Central Unit we can identify three main boards that account for power, data acquisition and data processing:

- **Acquisition Board:** its main function is the retrieval of raw data from the 3 sensors, data packaging, and high rate data transfer to the processing board. Detailed description is provided below.
- **Processing Board:** the Processing Board retrieves data packets from the acquisition board and performs on-board data processing. The processing board allows remote access and control of the unit from end users. Detailed description is provided below.
- **Power Supply Board:** The Central Unit requires 12V power. The Power supply board, deployed inside the central unit, provides power to the different boards and subsystems within the Central Unit.

Further additional subsystems within the Central Unit are:

- **Timing reference module (GPS):** the Central Unit is provided with a GPS module for time synchronization of the processing board. Both processing and raw data, saved in the internal memory of the processing board, are time stamped.
- **Communication system (WiFi/GSM):** The AshSizer is designed to operate remotely and to provide information on the volcanic fall-out in real-time. Several types of communications protocols have been considered while programming the processing board.
- **Local Service Interface:** The AshSizer is designed to operate remotely. Still, a local access is possible for local control through the local access interface, which allow to perform specific system administration tasks not accessible remotely.

- **Local USB Storage interface:** Both raw and processed data of an AshSizer sensor are available remotely. However, local download of processed results is possible through the local USB storage interface, with data copied automatically on a portable storage (like an USB key) once plugged in.

The choice of on-board processing was necessary as the AshSizer is designed to be deployed and operated in remote areas, with limited transmission bandwidth, thus preventing the possibility to transmit raw data and limiting remote access to processed results. Accordingly, the real “acquisition time” is thus controlled by the time necessary to transmit raw data from the acquisition board to the processing board and the time necessary to process these data. In the AshSizer prototype, that was delivered by M18 of the project, this was fixed in 10 seconds of acquisition every 30 seconds, with 20 seconds dedicated to data transfer and processing. This is a good compromise between data representativeness, with 8 hours of data acquired over 24 hours, data access and prompt response. Testing in the lab showed that the sum between transmission and processing time is approximately 12 seconds, thus leading to a redundancy of about 10 seconds, that is allowing the remote access and control of the processing board as well as remote data download.

### 2.2.2. Acquisition Board

As briefly described already, the Acquisition Board (Figure 8) retrieves data collected by the three sensors of the AshSizer, providing the weight of the collector, the level of the material inside the collector and the amplitude decay of the laser produced by particles passing through the Optical Barrier laser beam. Weight and level information is straightforward, and no signal conditioning or processing is required. Here data from the sensors is simply packaged into a specific data stream by the acquisition board and transferred to the processing board for data acquisition and sharing. The amplitude decay measured by the photo-detector, that allows retrieval of GSD and particle velocity of falling particles, needs specific data conditioning and a detailed description of that is provided in the following section.

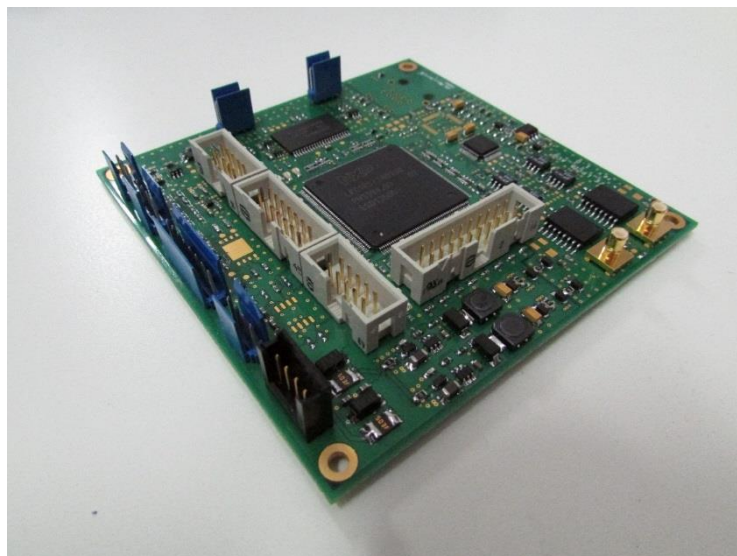


Figure 8: Picture of the Acquisition Board.

### 2.2.2.1. Optical Barrier Signal

A detailed description of the Optical Barrier is provided in section 2.1. Output is voltage, that is proportional to the laser intensity and thus reflects the amount of particles shadowing the laser beam (Figure 9). During its operation, the laser is modulated by the acquisition board at 30 KHz with a square wave amplitude resulting into an ON/OFF status. If no obstacles, such as ash particles, are present within the barrier, the optical detector will provide a square wave signal on its analog output. This square wave amplitude modulation results into a complex output signal, but it was necessary to minimize the ambient noise on the photo-detector.

During the ON state of the laser source, the presence of any ash particle (or other objects) within the barrier will produce a shading effect on the detector that will provide a proportionally decay of the output voltage (Figure 10). During the OFF state of the laser source, the optical detector signal level will be proportional to the level of the ambient light in the spectral range of the optical detector. Therefore, also in this case the presence of any particle will produce small amplitude decay on the optical detector (Figure 10).

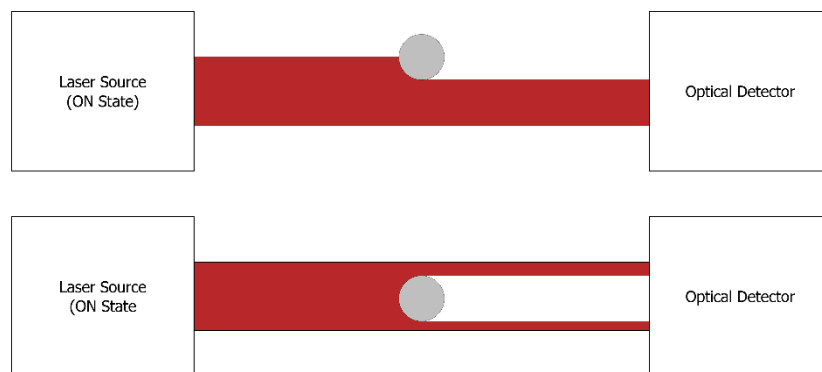


Figure 9: Laser Barrier working principle

The whole effect on the photo-detector output produced by a single particle crossing the laser beam is displayed in Figure 10 where the sensor output amplitude is displayed versus time. Here, the meaning of the figure labels are as follows:

- $L_H$  (high level) represents the amplitude of the photo-detector output when the laser is on. Its maximum level ( $L_{HM}$ ), that is recorded when no particles are crossing the beam such as for the first sample and last 3 samples of the time series of Figure 10, depends on sensor characteristics and alignment of the Optical Barrier and it is constant during sensor operation.
- $L_L$  (low level) represents the amplitude of the photo-detector output when the laser is off. As for  $L_H$ , its maximum level ( $L_{LM}$ ), is recorded when no particles are crossing the beam such as for the first sample and last 3 samples of the time series of Figure 10.  $L_{LM}$  depends on the ambient light in the spectral range of the photo-detector and is thus varying with day light, cloud cover and thickness of the ash cloud in the optical barrier.
- $A_1$  (high level attenuation) represents the attenuation measured by the photo-detector when the laser is on, and it is obtained from the difference of  $L_{HM}$  and  $L_H$ . It is proportional to the size of the particles that is crossing the beam at that specific time.
- $A_2$  (low level attenuation) represents the attenuation measured by the photo-detector when the laser is off.

The amplitude decay, representative of the shadow produced by the particle crossing the linear laser beam, is thus obtained from the difference between  $A_1$  and  $A_2$ . This allows to minimize the effect to ambient noise.

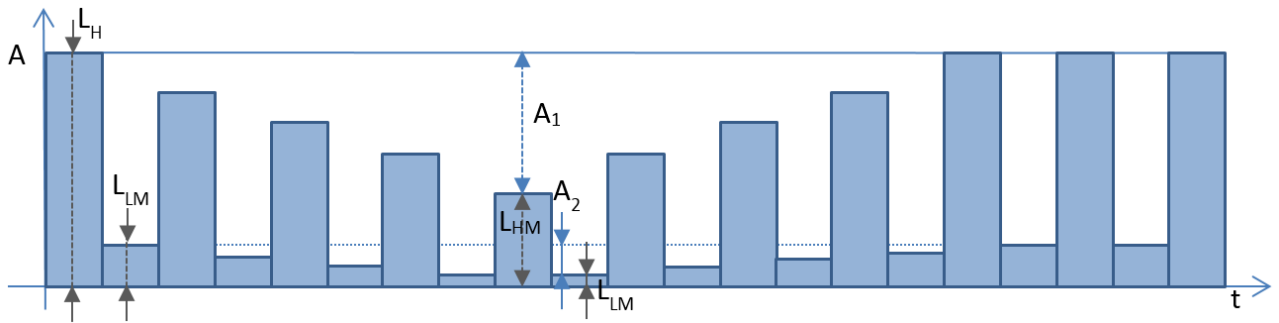


Figure 10: Particle crossing effect on the sensor output.

The typical feature of highs and lows expected from the analogue output of the photo-detector observed in Figure 10 is a result of the square wave amplitude modulation of the laser source. As explained above, this was required to minimize the ambient noise on the sensor itself. Accordingly, voltage output from the photo-detector needs to be acquired both for state ON and OFF of the laser, at the sampling rate of 30 KHz.

After initial tests and calculations about the expected dynamic range, minimum sampling frequency, and response of low-pass filter necessary to satisfy the Nyquist criteria for the noise we opted for a dual channel acquisition, with the analog signal coming from the laser barrier detector is applied to a couple of Sample & Hold that operate alternatively in order to store the end of the ON level during the OFF phase or the end of the OFF level during the ON phase as shown in Figure 11. This dual acquisition solution allows to reduce the settling time error of the filter as a consequence of the reduce amplitude difference between successive data points, thus making AD conversion much more reliable as would be achieved for a single acquisition channel (Figure 12)

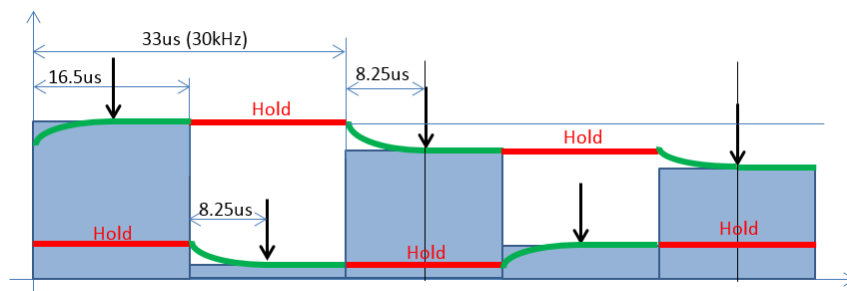


Figure 11 – Dual channel acquisition scheme, showing sampling (green) and hold (red) of the level of interest. In this case, given the limited amplitude difference between successive samples, the low-pass filter allows the quick recovering of the real amplitude.

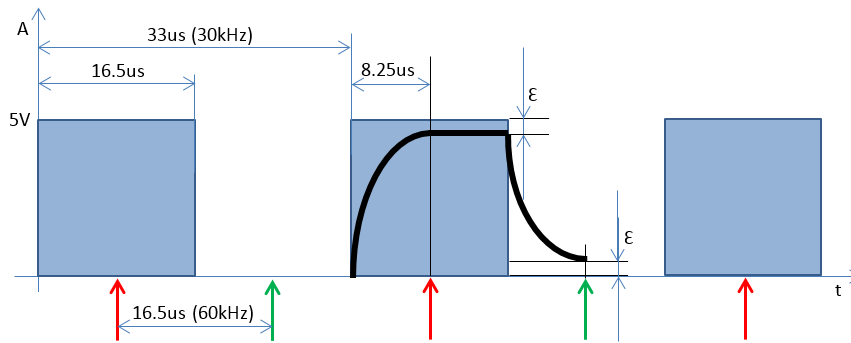


Figure 12: Acquisition chain settling time requirements. The low level sampling point is marked with a green arrow while the high level sampling point is marked with a red arrow. In this single acquisition configuration, the low-pass filter applied to the large dynamic range between two successive samples prevents the proper voltage output to be robustly recovered.

It is clear from the discussion presented above that the choice of the dynamic range of the AD converter, and the sampling rate is strongly related to the minimum size of the particles to be investigated and the maximum detectable terminal velocity. The area of the laser beam was fixed into  $48 \text{ mm}^2$  ( $30 \times 1.6 \text{ mm}$ ). Here, a spherical particle with a diameter of  $100 \text{ }\mu\text{m}$  (surface of  $7.9 \cdot 10^{-3} \text{ mm}^2$ ) would result into an obscuration of  $0.16\%$  that corresponds to minimum dynamic range of 13 bits. In the same way, the  $100 \text{ }\mu\text{m}$  ash particle would require  $1.6 \cdot 10^{-4}$  seconds to cross the beam when traveling at a terminal velocity of  $10 \text{ m/s}$ . Accordingly, we adopted a 16 bits AD conversion at the sample rate of  $30 \text{ KHz}$  to ensure the proper detection of terminal velocity up to  $10 \text{ m/s}$  and grain size as low as  $100 \text{ }\mu\text{m}$  diameter.

#### 2.2.2.2. Acquisition Board architecture.

The advantages that arises from this architecture are however not costless. Such method employs a couple of high performance sample & hold with 16-bit accuracy, a couple of matched response low-pass filters and finally a couple of high speed synchronous ADC. Such systems have to be synchronized together by using a high performance microcontroller. This arrangement is not available on the market; therefore it had to be design and developed as custom device.

In Figure 13 the acquisition board architecture is shown. The board is based on an high speed 16-bit microprocessor interfaced to a dual channel synchronized 16-bit ADC with sample rate up to  $500\text{kSps}$  by using parallel interface. The same microprocessor is interfaced with an additional volatile memory (RAM) that is used to perform the preliminary processing on the data coming from the laser barrier sensor. Finally, a couple of industrial standard serial interface (SPI and I2C) are used in order to connect the other sensor (level and load cell) to the microprocessor.

In Figure 8 the developed prototype is shown. In the middle is visible the 16-bit processor. The analog section (S&H, filter and converter) is hosted on the right part of the board. On the front side are visible the connector employed to interface to the sensor, to the power supply and to the processing board. The board is hosted on a  $100\text{mm} \times 100\text{mm}$  4-layer gold plated PCB.

Data collected (and processed) from the different sensors (Optical Barrier, level and weight) are eventually organized in a data package that includes the laser amplitude decay ( $300000$  samples @16 bits for 10 seconds of data) one data point for the level sensor (@16) and one data

point for the weight sensor (@16). Additional information is derived from the data stream from the Optical Barrier regarding the laser power and the external light, derived from the mean value of the high and low level respectively ( $L_{HM}$ ,  $L_{LM}$ ). This data stream is eventually sent to the processing board after every acquisition of 10 seconds by using a hi-speed ( $\approx 1\text{Mbps}$ ) RS232 serial interface.

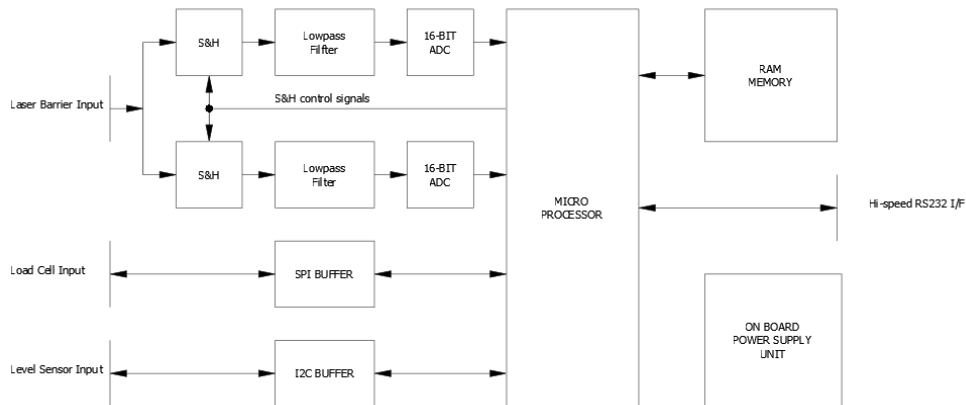


Figure 13: Acquisition board architecture

### 2.2.3. The Processing Board.

The processing board embedded in the Central Unit of the AshSizer allows remote real-time processing and network service capabilities. This required adopting a board able to support an embedded operative system. For the development of the AshSizer prototype, we used the Acmesys FOXBoard G20 (Figure 14), which is developed around the Atmel AT91SAM9G20 CPU, a 400MHz CPU based on the integration of an ARM926EJ-S processor with fast ROM and RAM memories. The FOXBoardG20 has a wide range of peripherals like an Ethernet interface, one USB device Port, one USB host controller and several standard peripherals, such as the USART, SPI, I2C.

A Debian/Unix operative system distributed for ARM cores was installed in the FOX Board G20 with an administrative tool able to retrieve e resolve package dependencies (software components) from the online software repository. The operative system is installed on a Secure Digital card hosted on board, which also non volatile data storage functions. The overall power requirement of this subsystem is less than 2W.

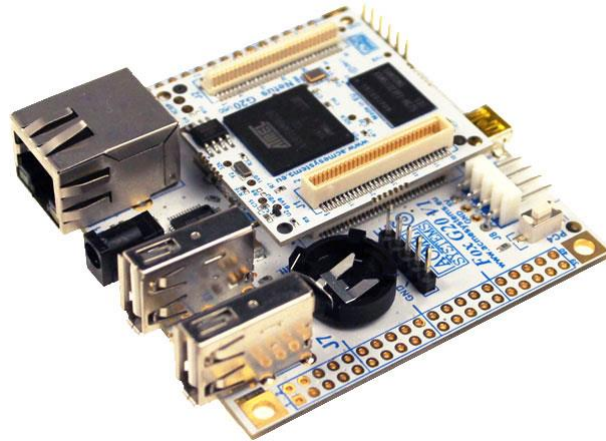


Figure 14: Acmesys FOXBoard G20 used in the AshSizer processing board.

In order to allow UTC time synchronization we included in the processing board a Skytraq GPS module which updates regularly the FOXBoardG20 clock.

In Figure 15 the processing board software architecture is shown. The raw data coming from the acquisition board are collected by a service called “Data Collecting Daemon” and locally stored in the SD card (Rawdata Storage on the same figure). Raw data are saved in a dedicated folder (1 file of 10 seconds of data every 30 seconds) with the format of the filename (YYYYMMDD\_hhmmss\_FVD.fvd) providing information of the UTC recording time. A further service called “Processing Daemon” has the task to gather the rawdata, to apply the statistical processing and to save the output in the SD card (Processed Data Storage on the same figure). Finally, a network file access service allow us to remotely access raw and processed data by using WiFi or GSM network. A brief description of each software module will be presented in the following paragraph.

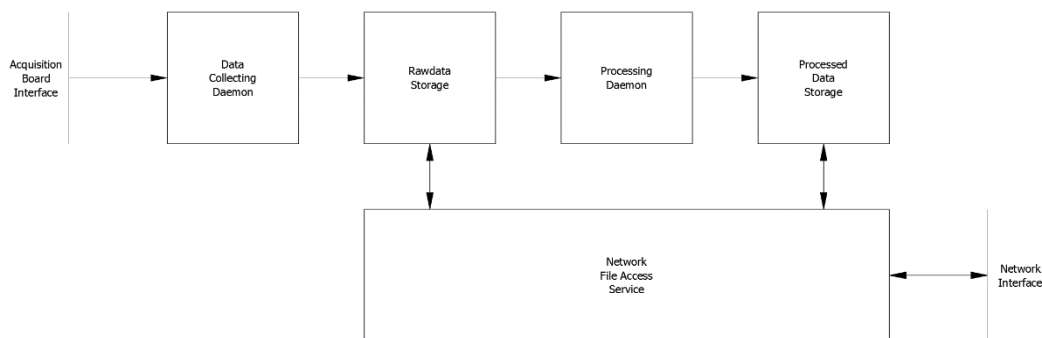


Figure 15: Software architecture of the Processing Board.

Raw data and processed data are available remotely by using the Central Unit network interface capability hosted on the Processing Board. Connection will be achieved with a GSM/3G router or a WiFi router depending local connectivity, with the remote access to the file system being platform independent. File access and real-time transfer of processing results is organized upon a client/server architecture, with the server being hosted on the Central Unit. Standard FTP

access service is available to all stored data (raw and processed). Download of raw data buffer is thus available remotely by using an FTP client or locally with a USB removable hard drive.

#### 2.2.4. Development of the first Central Unit prototype

The AshSizer hardware and software modules (Acquisition Board, Processing Board, Power Supply Board etc.) were integrated together in order to develop the Central Unit that is embedded in the prototype delivered by M18 (Figure 16) below the ash collector within the Collector Unit.

The whole system is hosted in a 240 x 200 x 110 mm die casted aluminum case with IP 67 environmental grade protection. The processing and acquisition board was stacked up together in order to reduce their footprint and firmly anchored to the box by using a suitable metal plate.



*Figure 16: Inside view of the AshSizer Central Unit.*

Connectors are positioned both in the front panel (weight sensor, level sensor, GPS antenna, USB e RS232 interface, 12 V power) and in the rear panel (Ethernet, Optical Barrier connector, USB data storage) with 400 Series Buccanner Bulgin connectors (Figure 17). Three light indicators are used in order to display the status of acquisition board (red), processing board (green) and GPS module (blue), which provide the status of the subsystems locally.

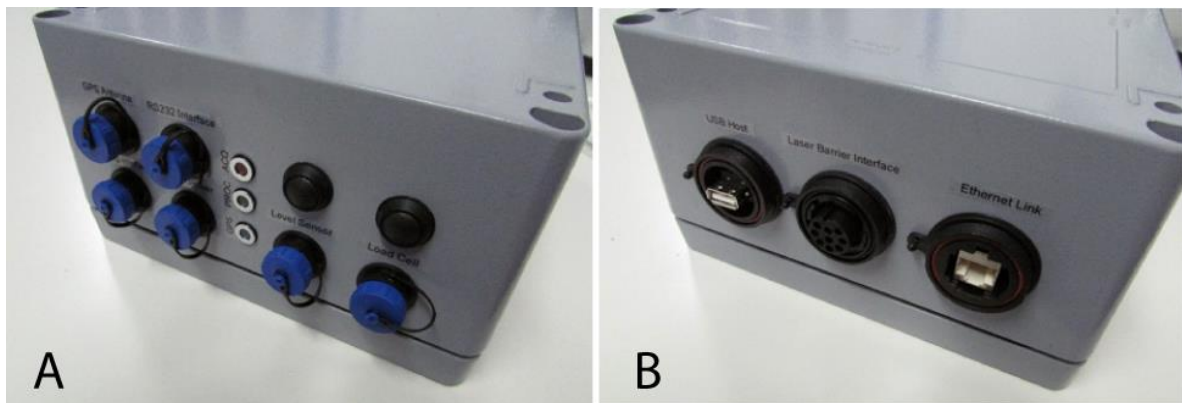


Figure 17: View of the front (A) and rear (B) panels of the Central Unit embedded in the sensor Connector Unit.

### 2.3. AshSizer Calibration

Various tests have been performed during the first year of instrument development of the sensor (Oct 2012- Sept 2013). These tests focused mostly on the Optical Barrier (Figure 18) and were performed by using metal spheres (1 and 2.5 mm diameter) that allowed projecting and optimizing further instrument developments such as the type of photo-detector to be used (single photo detector instead of an array), the optimal size of the linear laser beam and the architecture of the acquisition board (dual AD conversion with sample & hold) that have been described in the previous section of the present report.

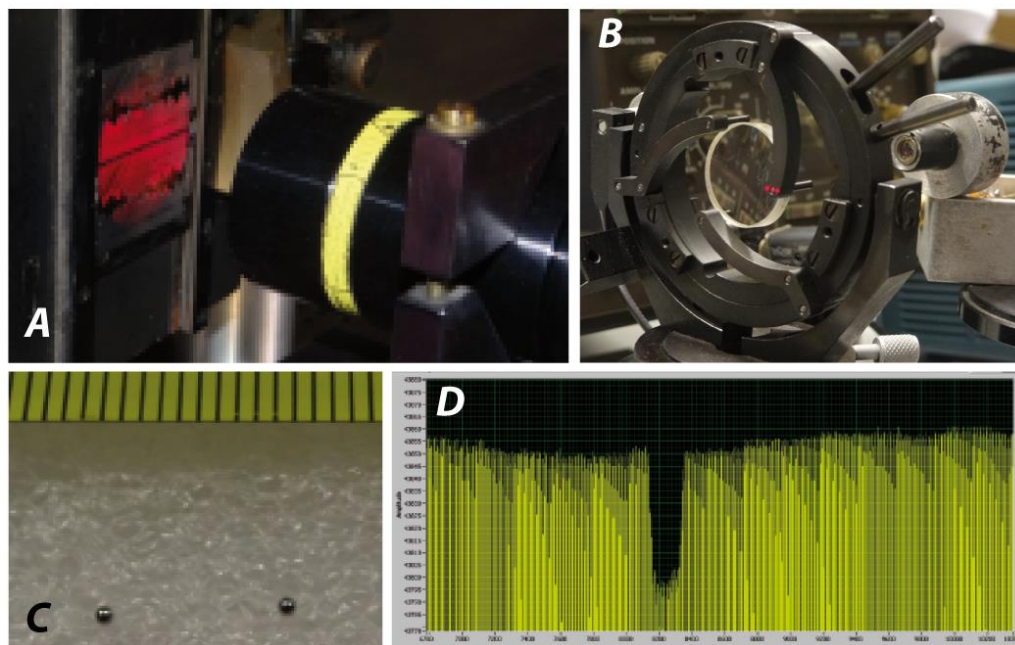


Figure 18: Picture of the laser and the laser window (A), the lens and photo-detector (B), 1mm diameter spheres, and sample of acquisition at 50 KHz showing the amplitude decay of such particles crossing a 5 mm beam. Time duration of the amplitude decay is consistent with a terminal velocity of 1.37 m/s.

A more proper calibration of the AshSizer collector was performed starting M18 of the project, when the prototype was delivered, as the acquisition and processing board as well as the mechanical features of the instrument (thickness of the linear beam, filter, type of photo-detector) had been eventually realized. Calibration tests allowed both to verify the sensor

sensitivity and resolution and to tune the on-board processing. However, because of logistical reasons in the laboratory (ash amount, mutual position of the Optical Barrier and collector etc.), the optical barrier and the collector (weight and level sensors) were calibrated in the laboratory separately, and further calibration will be required in the field during ongoing volcanic ash emissions, in order to test the whole sensor response in the real environment.

### 2.3.1. Calibration of the Optical Barrier

The expected amplitude decay of spherical particles can be evaluated theoretically once the dimension of the linear laser beam is known (Figure 19) from the relative size of the particle crossing the beam. However, ash particles commonly depart from the spherical assumption, with varying aerodynamic properties, shape and vesicle content of single grains (Figure 20). For this reason, the calibration of the Optical Barrier was performed in the laboratory with real ash, characterized by grain size ranging between  $\Phi = -1$  and  $\Phi = 3$  ( $\Phi = -\log_2 D$ , where  $D$  is the particle diameter in millimeters) collected from a tephra deposit from the XVIII Century vulcanian activity of Vulcano island (Italy).

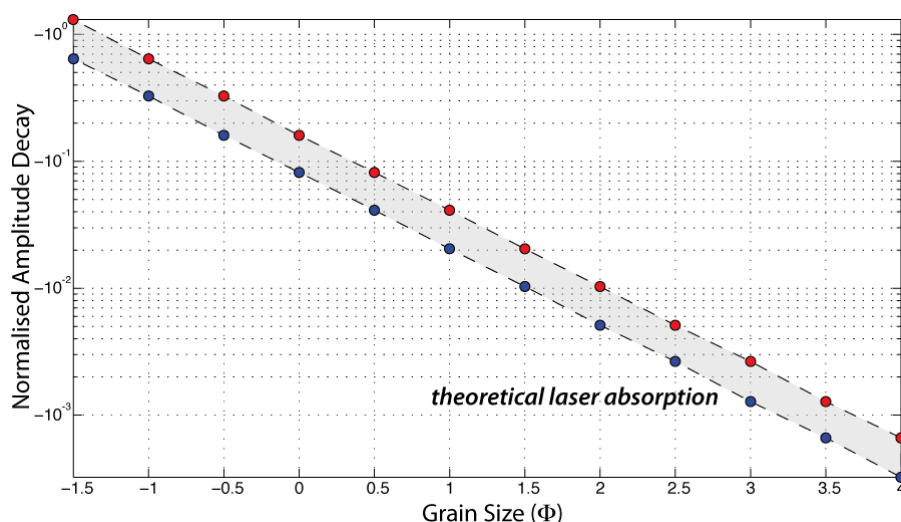


Figure 19: Theoretical normalized amplitude decay as measured from the photo-detector for spherical particles crossing the linear laser beam as a function of grain size ( $\Phi$ ). Red and blue dots represent the largest and smallest particles within each single class.

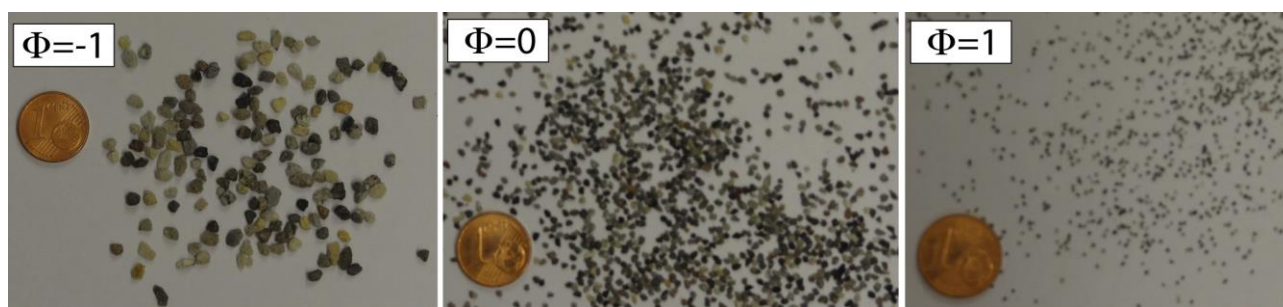


Figure 20: Pictures of ash grains from three different classes mechanically dry-sieved from a real tephra deposit from Vulcano (Italy), belonging to the Pietre Cotte Cycle (XVIII Century) and used in the calibration of the Optical Barrier.

The ash had been mechanically dry-sieved at half- $\Phi$  intervals, with each class grouping particles within a minimum and maximum range of grain diameter (Table 1). In order to evaluate

experimentally the mean amplitude decays particles of a given dimension class have been thrown across the linear laser beam. This was achieved mechanically with a speaker in order to keep the fall out rate as stable as possible.

Amplitude decays related to particles from a single class crossing the beam tend to have a Gaussian distribution peaked around the median values of maximum and minimum expected decay, with the tail of the distribution exceeding the minimum and maximum theoretical values. This is possibly to be explained with the departure of real particles from the spherical shape, that crossing the beam are producing an actual amplitude decay of the output from the photo-detector that depends from the particle orientation. The amplitude decay for single  $\Phi$  classes, between  $\Phi=-1$  and  $\Phi=3$  was thus evaluated experimentally providing threshold values that are summarized in Table 1.

Table 1: Maximum and minimum diameter and corresponding measured normalized amplitude decay from the Optical Barrier photo-detector for different classes of particles.

Grain Size ( $\Phi$ )	Grain size range ( $\mu\text{m}$ )	Measured Normalised Decay
-1	4000-2000	0.9-0.95
0	2200-1000	0.95-0.98
1	1000-500	0.98-0.994
2	500-250	0.994-0.998
3	250-125	0.998-1

In order to test the experimental threshold values (Table 1) several tests were performed by measuring a mixture of variable amounts of particles from the different grain size classes available passing through the laser beam of the Optical Barrier. Figure 21 shows the distribution of normalised amplitude decay for particles that passed through the optical barrier laser beam during a 30 minute-long measurement performed on March, 13<sup>th</sup>, 2014. Among the 117900 particles, that were detected by the Optical Barrier as causing a decay of the photo-detector analogue output, apparent cluster of particles appear to show a Gaussian distribution of amplitude decay that appear consistent with experimental threshold.

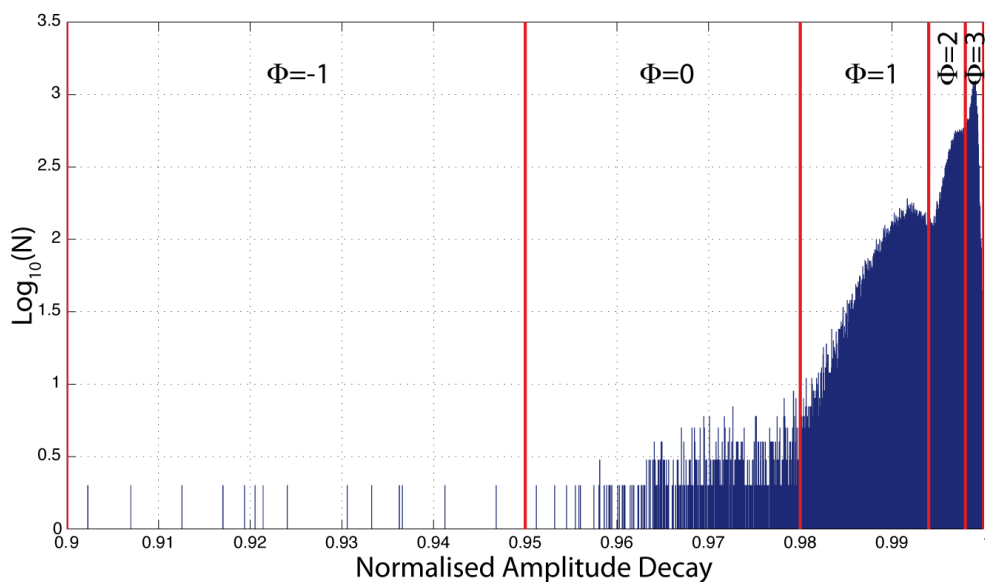


Figure 21: Normalised amplitude decay distribution for a mixture of particles with different grain size as measured by the Optical Barrier. The 5 classes of interest are highlighted and number of particles with a given decay is shown.

From the measured distribution (Figure 21) the grain size distribution (GSD) of fall-out material could be evaluated, both in terms of percentage of particles of a given class (Figure 22a) or percentage of volumes for the different classes (Figure 22b). The latter is evaluated by multiplying the number of particles for the mean volume of each particle from a given class of grain size.

In order to validate the results obtained from the analysis of the amplitude decay related to laser obscuration, the fall-out material collected during the experiment was mechanically sieved again and GSD, in terms of total weight, was calculated (Figure 23). The total volume distribution shown in Figure 22b is converted into weight by applying a constant density of  $1500 \text{ kg/m}^3$  evaluated from the weight and thickness of the collected material. The comparison (Figure 23) is strongly promising showing a good match for larger classes and a limited misfit for the smaller class taken into account. It is to be considered that particles detected by the AshSizer Optical Barrier in not fully coincident with the collected fall-out material that was eventually mechanically sieved and used for calculating the GSD. The reason is that the Optical Barrier operated 10 seconds every 30 seconds, in order to allow data transfer and on-board data processing as described in the previous section, while material fall-out was constant during the whole duration of the test.

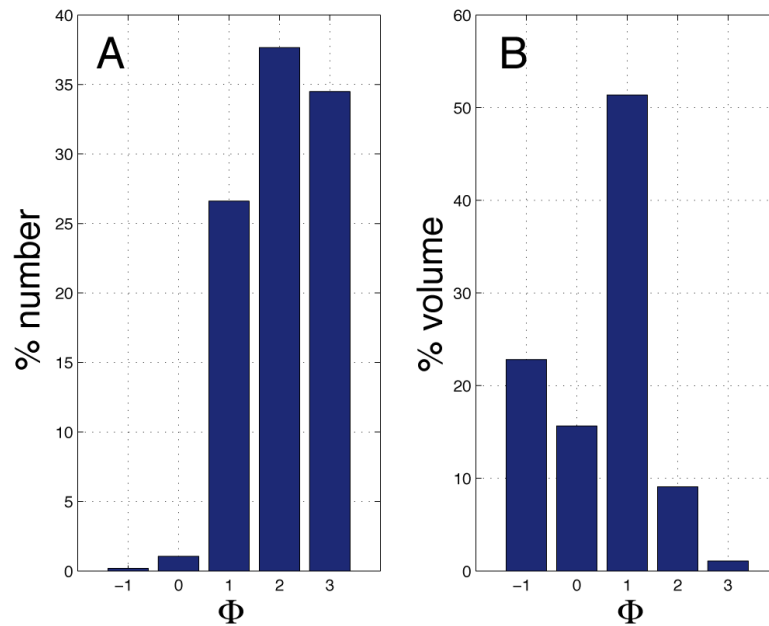


Figure 22: Grain Size Distribution of a mixture of particles from 5 different grain size classes ( $\Phi = -1:3$ ) as measured by the AshSizer sensor. The distribution is expressed in terms of percentage of the number of particles (A) or percentage of the total volume of the different classes of particles (B).

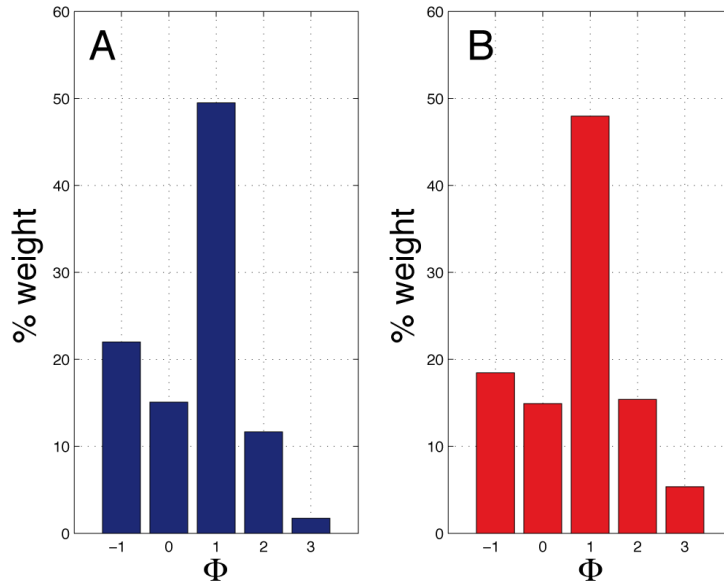


Figure 23: Comparison of GSD (in terms of weight) measured from the AshSizer (A) and measured after mechanical sieving of collected fall-out material (B).

### 2.3.2. Calibration of the Collector Unit

As described already in section 2, the collector unit is equipped with a load cell and level sensor, that provide in near real-time the weight and thickness of material accumulating in the sensor collector (Figure 2a). During the calibration phase of the AshSizer, the two sensors have been tested in order to evaluate properly the sensitivity and resolution.

The collected ash weight is provided by a load cell (CZL635) operating in the 0-5 kg range with a nominal resolution of 1 g. In order to test the sensor sensitivity, a known amount of water was added in the ash collector, with measurement being performed by the acquisition board every 30 seconds (Figure 24). One cubic centimeter of water (1 gram) was added every 30 seconds during the 15 minutes of the test (green in Figure 24), the same weight was measured for 5 minutes (red in Figure 24) and 2 CC of water (2 grams) were eventually added every 30 seconds for the rest of the calibration test (blue in Figure 24). This shows that a weight increase of 1-2 grams can be detected robustly by the load cell.

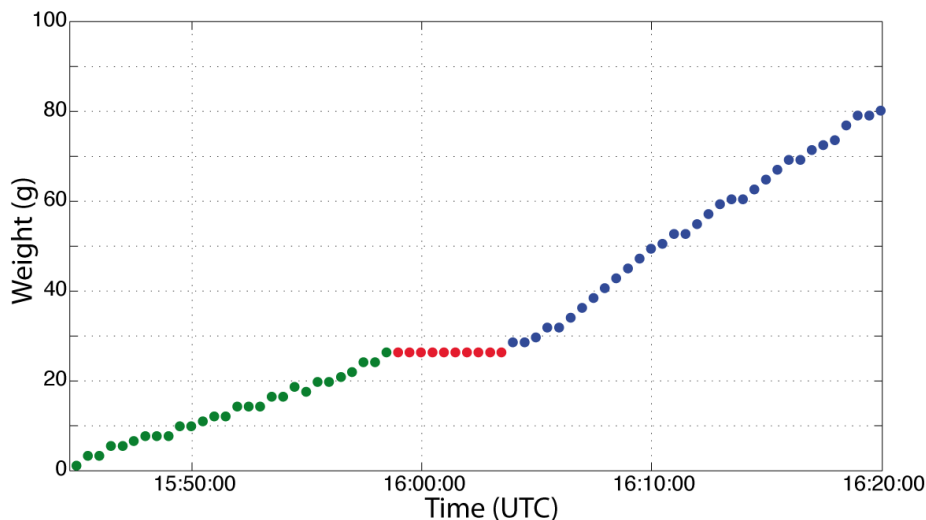


Figure 24: Calibration of the weight sensor realised by adding known amount of water every 30 seconds (1 g, green; 0 g, red; 2 g, blue).

In addition to the weight, the level of the ash inside the collector is measured with an ultrasound sensor (SRF235), measuring the two-way distance from the sensor to a reflecting surface in the 10-120 cm range. Operating at 235 KHz and with a reflection with a beam of 15°, it is strongly range limited but ensures a resolution of ~ 1 mm. The 80 g of water added in the collector during the calibration experiment (Figure 24) resulted into a 2 mm thick level of water within the collector, given the diameter of 20 cm and the water density of 1000 kg/m<sup>3</sup>. However, the surface tension of the water prevented the formation of a homogeneous level. Accordingly, in order to test the resolution of the level sensor, we show here the measurement of 790 g of water within the collector, that resulted into a vertical distance of 26.27 cm between the sensor and the water surface (Figure 25), assuming a 345 m/s propagation velocity of the emitted and reflected acoustic wave. While the weight measurement is extremely stable, the level measurement appears to vary between 26.2 and 26.35, thus validating the nominal resolution of +/- 1 mm. Assuming a tephra density of 1500 kg/m<sup>3</sup>, a increase of 1 mm of ash in the collector would correspond approximately to 50 g of material accumulating within the collector.

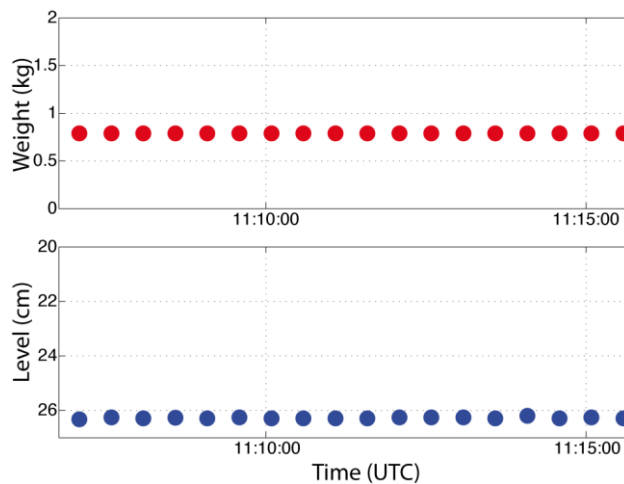


Figure 25: Weight (red) and level (blue) measured for 790 g of water within the collector. The level measurement peaks at 26.27 cm (range 26.2-26.35) is indicating a resolution of the level measurement of +/- 1 mm.

Figure 26 shows a test of water accumulating within the collector with both level and weight measured at the same time and with picture showing the level of water within the collector for the different measurement steps.

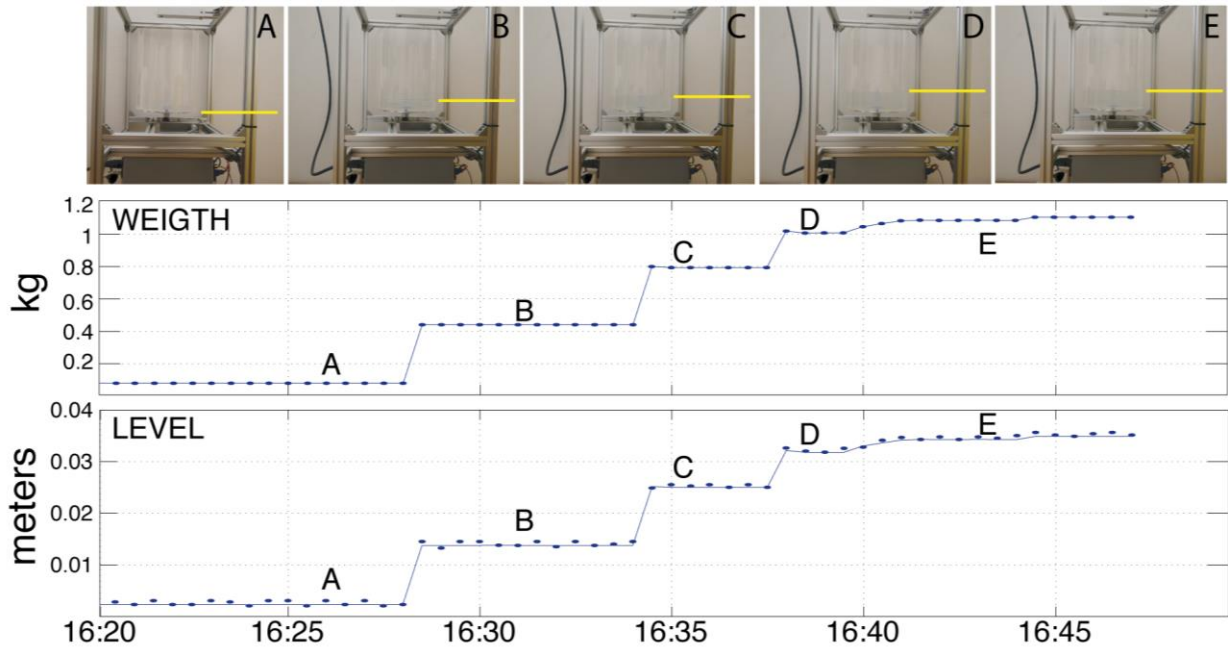


Figure 26: Picture of different amount of water filling the collector and corresponding weight and level measurement.

## 2.4. AshSizer client

AshSizer is designed to produce one measurement every 30 seconds. Each measurement is stored in the internal memory and is also real-time broadcasted over the internet. Data can be visualized using a stand-alone application developed by Item s.r.l. with the instrument (AshViewer). A web-console is also implemented to check if the AshSizer is properly working, to download the data, and to set the network configuration. This section will introduce the Web Console functionalities, AshSizer output data format, and how to handle the acquired data using AshViewer software.

### 2.4.1. Web Console

AshSizer web-console is hosted by default on <http://192.168.0.12/ash/> (Figure 27). The web page shows the raw output results of the last acquisition (top left) and the current GPS status (top right). The system can be checked that is properly running if the raw output results are refreshed every 30 seconds. Raw output data format will be detailed in the following section.

To control the instrument time drift and to detect the instrument position, AshSizer is equipped with on-board GPS allowing us to control the correct time stamp of each measurement. From

web console it is possible to check if the system time is correctly set when SHM voice is flagged with a cross (+) or a star (\*).

Web console allows also to download the stored data in the internal memory: by clicking on “Download Results” the processed data file is downloaded, from the Central Unit, where all the measurements are saved, while by clicking on “Download Raw-data” it is possible to access to the rawdata records of the acquisition board.

Using web-console it is also possible to change the AshSizer network configuration in terms of IP address, Netmask, Gateway, and DNS server, or to set AshSizer in DHCP mode. Finally, by clicking on “Reboot” button the system is forced to make an hard reboot.

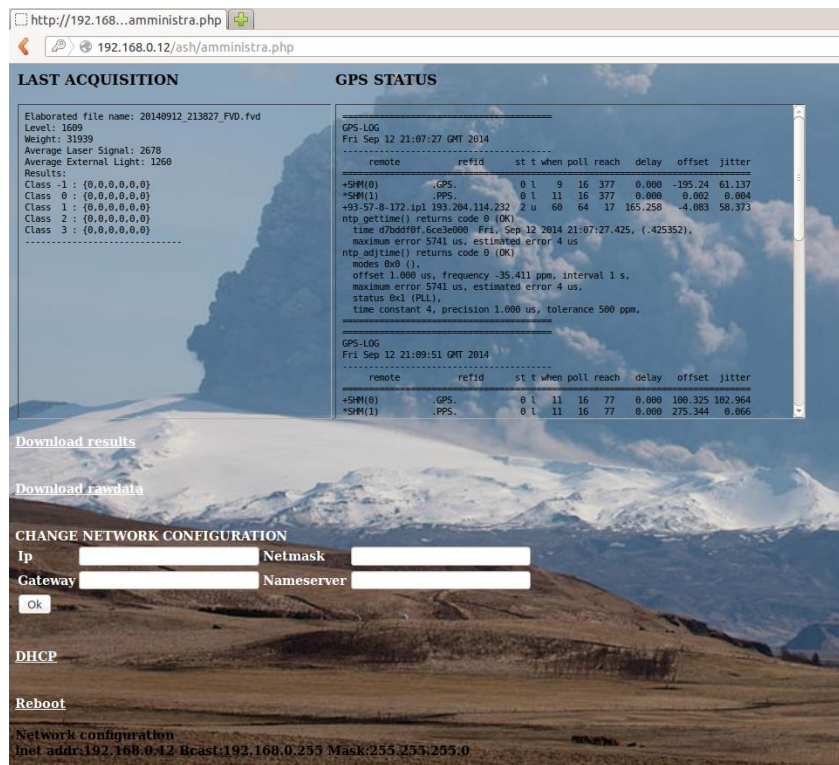


Figure 27: AshSizer web-console, showing last acquisition data, the GPS status, and allowing to download data and change network settings.

### 2.4.2. Output Data Format

AshSizer output data format consists in a 12 lines ASCII string where all raw measurements are displayed (Figure 28). First line shows the filename associated with raw records from acquisition board that has been processed. Filename is timestamped using YYYYMMDD\_HHMMSS format, where YYYY is the year, MM the month, DD is the day, HH is the hour, MM are the minutes, and SS are the seconds associated with the acquisition time.

Second line shows the ash height measurement as given by the level meter. This measure is given in counts and labelled with **Level**. Using the following formula it is possible to calculate the height in centimetres:

$$Height[cm] = \frac{Counts}{2 * 10^6} * 34500$$

Third line shows the ash weight measurement as given by the weight sensor. This measure is given in counts and labeled with **Weight**. Using the following formula it is possible to calculate the weight in grams:

$$Weight[g] = \frac{Counts - 31943}{0.9102}$$

Fourth, fifth and sixth lines show three parameters that are useful to check if the laser unit is properly working. **Signal level** parameter is associated with the intensity of the beam that is received by the optical detector. This parameter is dependent to the output laser intensity and to the alignment between the laser beam and the detector. **Noise level** parameter is dependent to the intensity of the background ambient scattered light that changes in intensity during the day and accordingly with atmospheric condition (fog, rain, etc...). **RMS Amplitude** parameter gives information about the accuracy and the proper functionalities of the light detector. RMS Amplitudes above 0.01 might indicate a mis-alignment of the laser unit, or instrumental noise due to detector damages. High RMS Amplitudes (>0.01) lead to false detections in the lower size particles.

The following lines labelled with **Results** show the output results given by the automatic particle counting algorithm applied to laser unit output signal. All detected particles are organized into grain size classes using  $\Phi$  scale (from  $\Phi = -1$  to  $\Phi = 3$ ) and into terminal velocity classes (from <0.1 m/s, 0.1-0.5 m/s, 0.5-1 m/s, 1-2 m/s, 4-6 m/s, >6 m/s) and thus resulting in an array sized 6 rows (terminal velocity classes) x 5 (grain size classes).

```

Processed file: 20140923_010013_FVD.fvd
Level: 1143
Weight: 32139
Signal Level: 2731
Noise Level: 800
RMS Amplitude: 0.002256
Results:
Class -1 : {0,0,0,0,0,0}
Class 0 : {0,0,0,0,0,0}
Class 1 : {0,0,0,0,0,0}
Class 2 : {0,0,0,0,0,0}
Class 3 : {0,0,0,0,0,0}
-----

```

Figure 28: AshSizer output data format associated with a single measurement.

### 2.4.3. AshViewer

AshViewer is a stand-alone application developed in MATLAB and PYTHON environments and designed for display both real-time data stream (real-time mode) and data files downloaded from the AshSizer (offline mode). Using real time mode AshViewer acquires real-time data from the internet and saves them into the local hard drive. Real time mode is thus designed for monitoring application in case the user needs to have an automatic real time information update of ash fall-out. Using offline mode, the user can display and browse past data downloaded directly from the station. In both modes, AshViewer displays data into main two graphic windows (Figure 29, Figure 30): the statistic window and the time window. The Statistic window shows the grain size and terminal velocity distributions within a time span (usually 15 minutes) that can be set by the operator. This allows a fast visualization of the current characteristics of ash fall out. On page bottom last cumulative ash weight and level from ash collector is also shown. On bottom right some data information are displayed such as the time interval of analysis, the GPS position of instrument, and the last measured thickness and weight from the ash collector.

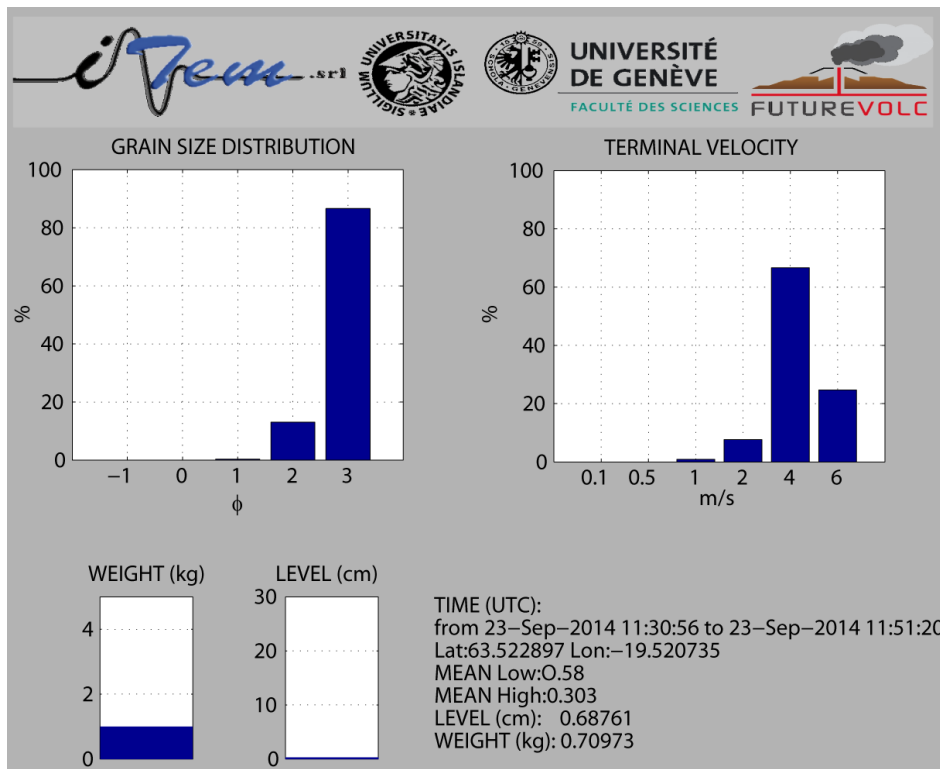


Figure 29: AshViewer statistic window showing real time grain size and terminal velocity distributions, weight and thickness of ash collector.

Real time window shows the results from every single 30 seconds of acquisition in terms of grain size distribution and terminal velocity distribution of the particles, and every weight and thickness measurements from ash collector, within the time span of analysis. This visualization allows to follow evolution through time of the intensity and parameters of ash fall-out and thus is useful for monitoring operations. Ash grain size and terminal velocity relative distributions are displayed using false colours (from dark blue, indicating 0%, to dark red, indicating distribution peaks).

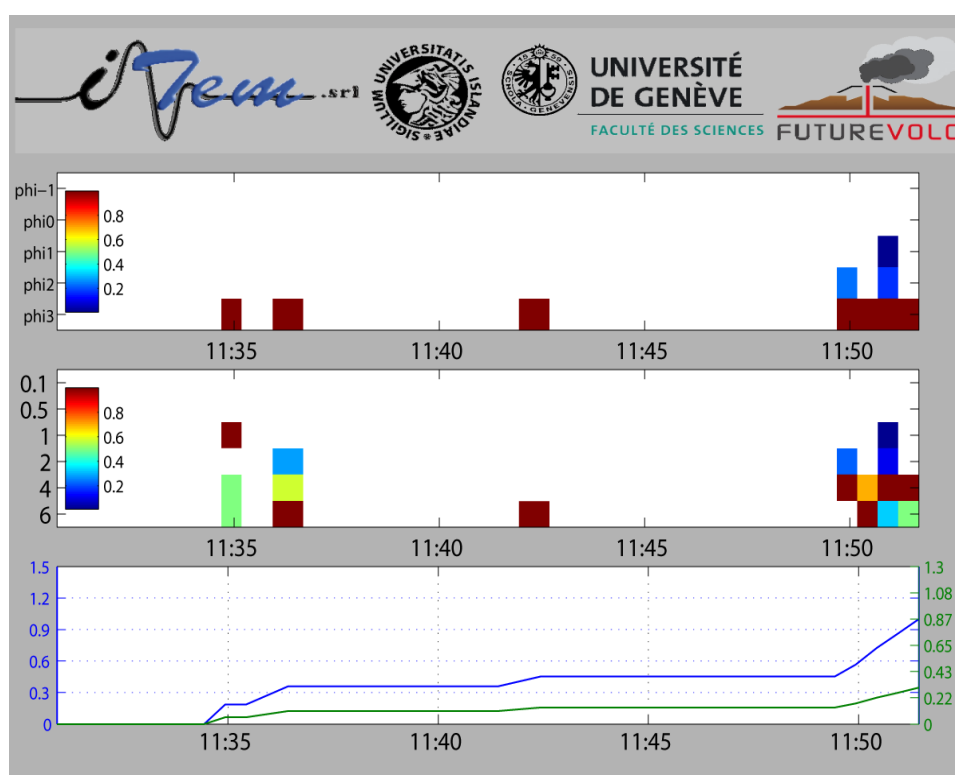


Figure 30: AshSizer real-time window showing ash grain size distribution, terminal velocity distribution, ash weight and level associated with every single measurements. This allows to follow evolution through time of the intensity and parameters of ash fall-out.

## 2.5. Future steps in the AshSizer development

During the first 24 months of collaborative work within the FUTUREVOLC project, Item s.r.l., in cooperation with the University of Geneva, University of Iceland and University of Firenze, has designed and developed the prototype of the AshSizer sensor, a ground based instrument designed to be operated remotely within volcanic plumes able to measure grain size distribution and terminal velocity of fall out material as well as fall out rate (weight and

thickness) and provide results remotely in near real-time. Single site measurements of Grain Size and thickness of tephra fall-out will be used to calculate TGSD and volume of tephra deposit based on dedicated strategies.

In order to accomplish the expected requirements of the AshSizer, several technical solutions had to be developed, both concerning the structure of the instruments and the electronics (embedded real-time processing etc.), which required changes and tuning of the instrument original project.

Laboratory tests were performed mostly between M18, when the prototype was delivered, and M24, when the prototype was presented at the second FUTUREVOLC annual meeting. A proper field test of the instrument is still missing, but the AshSizer prototype was left in Iceland after the second annual meeting, in case the current volcanic unrest evolves into an explosive phase and field test becomes feasible.

The AshSizer instrument was also used during the FUTUREVOLC EXERCISE that was performed on June, 18<sup>th</sup>, 2014. In that specific case the instrument was used in the laboratory of Item s.r.l. as if it was deployed in the field, in Iceland, and the scenario of the 2010 eruption of Eyjafjallajokull was simulated. Figure 31 shows results provided in near real-time, by simulating Eyjafjallajokull eruption with real ash collected at the time of the eruption in Skogar, at a distance of ~ 12 km from the eruptive vent, and measured by the instrument in the lab. The GSD reflects the real grain size of the ash sample, consisting mostly in fine ash ( $\Phi=2$ ), while the measured terminal velocity is strongly controlled by the experimental conditions. Latitude and longitude in Figure 31 simulate the field location (Skogar, Iceland), while operation time (15 minutes acquisition, on June, 18<sup>th</sup>, 2014), total weight of collected material (6 g) and fall-out rate (1.5 g/m<sup>2</sup>/s) are derived from the AshSizer real-time observation.

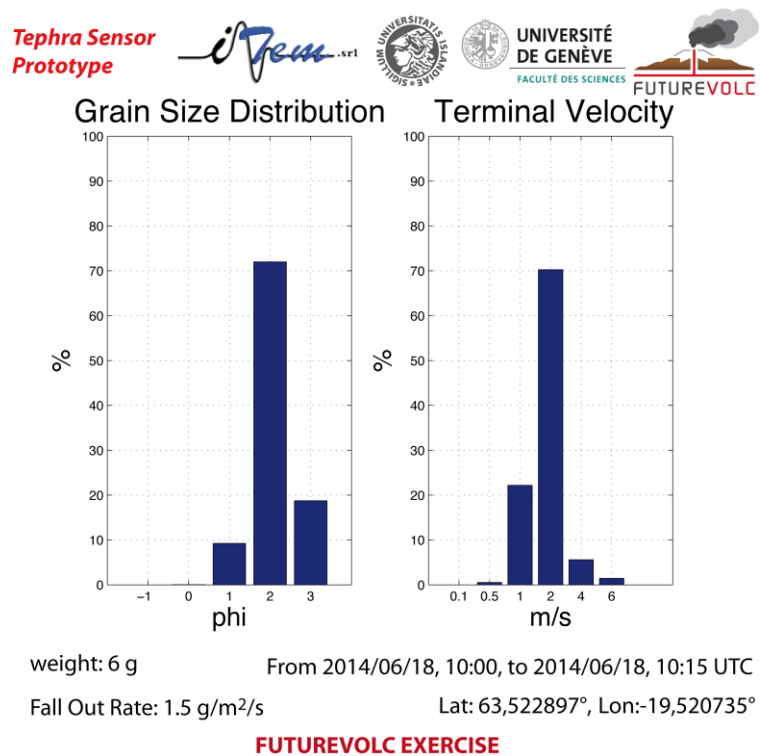


Figure 31: Sample of the information provided by the AshSizer during the June, 18th, 2014, FUTUREVOLC exercise.

Tests performed and results achieved so far are strongly encouraging and promising. GSD is obtained in real-time for grain sizes spanning from  $\Phi=1$  nad  $\Phi=3$ , terminal velocity is measured up to  $\sim 10$  m/s, weight is measured with a resolution of 1 g and ash thickness in the collector with a resolution of  $\pm 1$  mm. Processing is performed on-board and results are available in near real-time (every 30 sec) remotely.

At the time of this writing, Item s.r.l. is starting the production of sensors to be delivered in 6 months in the framework of the FUTUREVOLC project. These instruments will differ from the prototype mostly for the stainless steel structure both for the Optical Barrier and the Collector Unit, required for a proper field installation. Minor changes from the prototype will affect the Acquisition and Processing board, such as including a larger number of classes in the evaluation of GSD ( $\Phi/2$ ) and terminal velocity. Moreover, a decrease of the thickness of the linear laser beam (from 1.6 mm to 1 mm) will be tested in order to improve the sensitivity in grain size resolution for smaller particles ( $\Phi=3.5$ ).

### 3. The FUTUREVOLC infrasound arrays

In the framework of the FUTUREVOLC FP7 European Project, 3 small aperture infrasound arrays are being deployed in Iceland (Figure 32). The three arrays add to an existing small aperture array operated permanently since 2010 in Gunnarsholt (ICE 1). Two out of the 3 FUTUREVOLC arrays have been installed during the first 2 years of the project (ICE 2 in June 2012 and ICE 3 in May 2013) and are transmitting data to the UNIFI and IMO where real-time processing is performed. The infrasound arrays are used to provide real-time parameters of ongoing volcanic eruptions (timing of the event, source position and energy spectrum). The ultimate aim is to provide a real-time estimate of the Mass Eruption Rate inferred from infrasound observations. At the moment the 3 arrays target the East Volcanic Zone, with at least 1 array deployed within 100 km from the main active volcanoes. The last infrasound array (ICE4) was installed immediately after the second FUTUREVOLC annual meeting at close distance from Askja volcano in order to monitor the ongoing eruptive activity.

#### 3.1. Instrumentation and deployment of FUTUREVOLC arrays

All infrasound arrays are equipped with differential pressure transducers, with a sensitivity of 25 mV/Pa in the spectral range of 0.01-20 Hz within the +/- 100 Pa pressure range and instrument self noise is typically -50 dB rel 1Pa<sup>2</sup>/Hz (Figure 33). The different arrays have all the same installation geometry and similar aperture (maximum distance between elements of the array), while copper cables or fiber optic cables is used to connect the elements of different arrays. A detailed description of the different arrays is provided below.

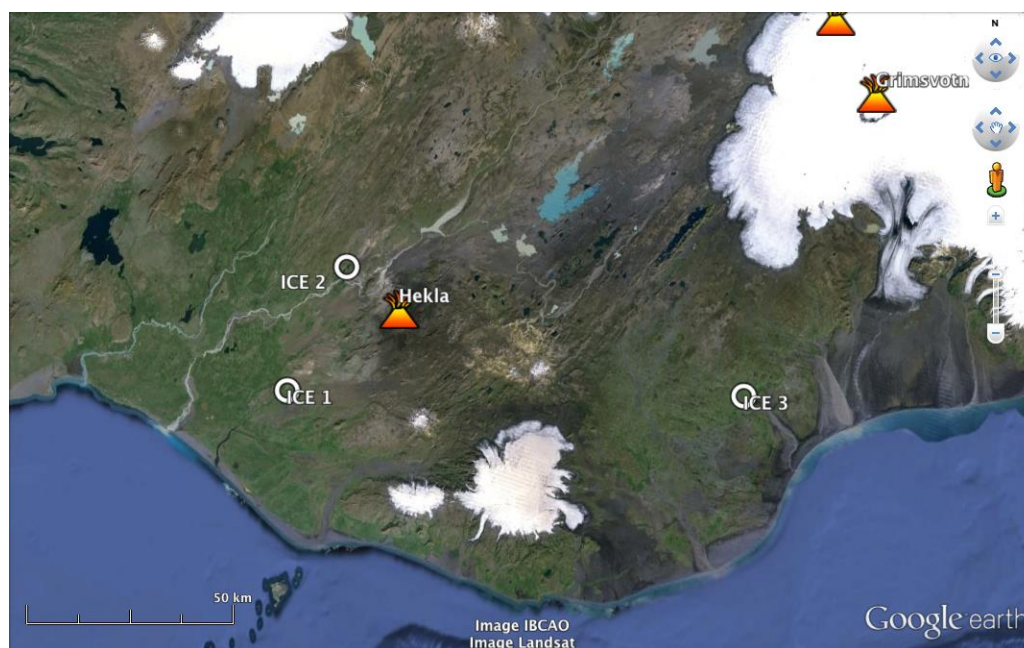


Figure 32: GoogleEarth view of the position of the 3 arrays installed in Southern Iceland.

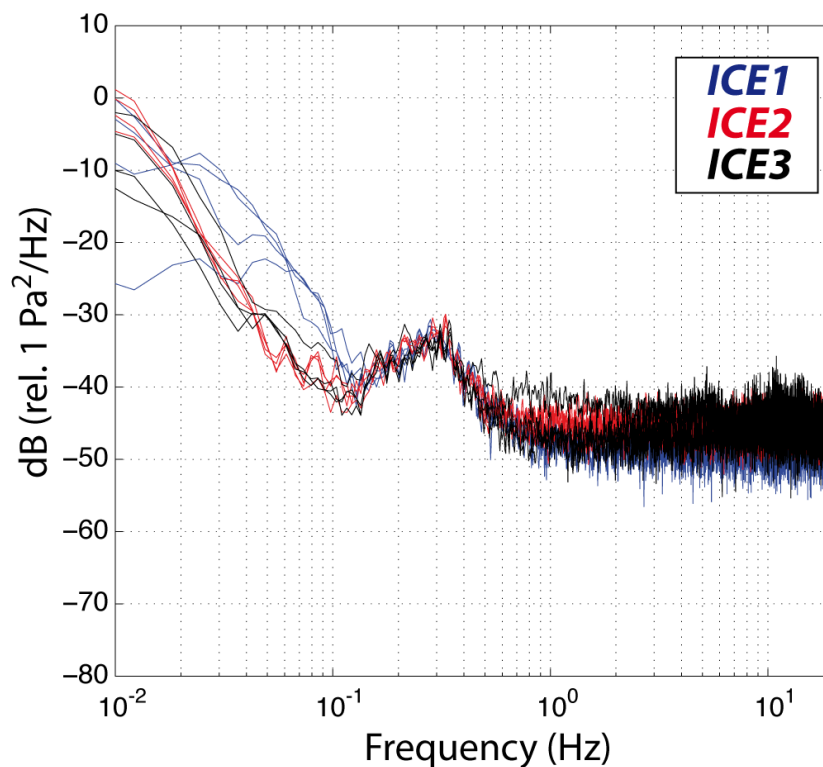


Figure 33: Power spectral density of infrasonic noise at the different elements of the 3 infrasonic arrays.

### 3.1.1. ICE 1 Array

Operating since May 2010, the ICE 1 array is installed in Gunnarsholt (Figure 34), at a distance of ~30 km from Hekla and ~ 40 km from Katla. The array is equipped with 4 differential pressure transducers (0.001-100 Hz, with +/- 100 Pa dynamic range) and a Guralp CMG/DM24 digitiser. Connection among the elements of the array is obtained with copper cable. GPS time stamped data are both recorded locally and transmitted with a UMTS/3G modem. Data is recorded in Iceland at the IMO and forwarded to the University of Firenze, in Italy, for real time processing.

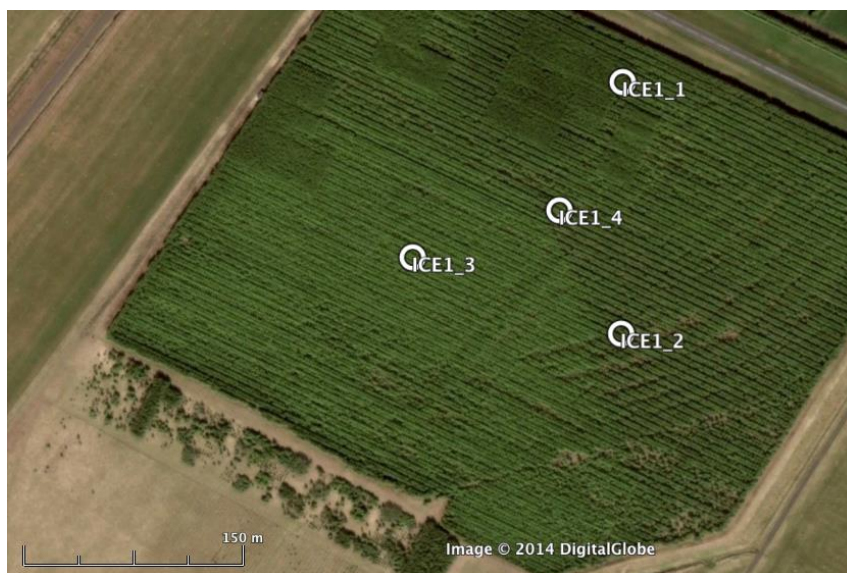


Figure 34: GoogleEarth view of the position of the elements of ICE1 array in Gunnarsholt.

### 3.1.2. ICE 2 Array

Operating since June 2013, the ICE 2 array is installed close to the town of Arnes (Figure 35), at a distance of  $\sim 18$  km to Hekla volcano, while Eyjafjallajökull and Katla are within a source-to-receiver distance of 70 km. The array consists into a FIBRA infrasound array, equipped with 4 digital differential pressure transducers (0.001-100 Hz, with  $\pm 100$  Pa dynamic range) connected with fiber optic cables (50/125  $\mu\text{m}$ ) to the central unit, where data is stored locally in a 2GByte SD card and transmitted with a UMTS/3G modem. Data is recorded in Iceland at the IMO and forwarded to the University of Firenze, in Italy, for real time processing.

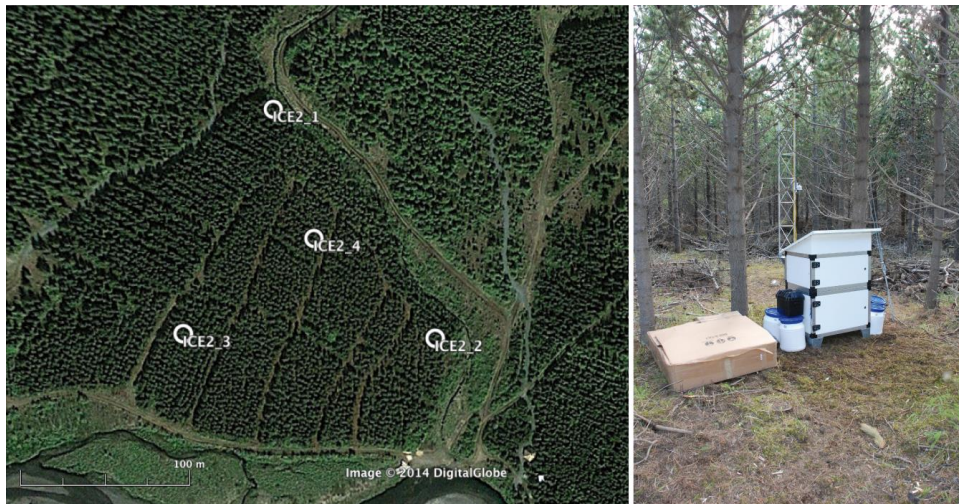
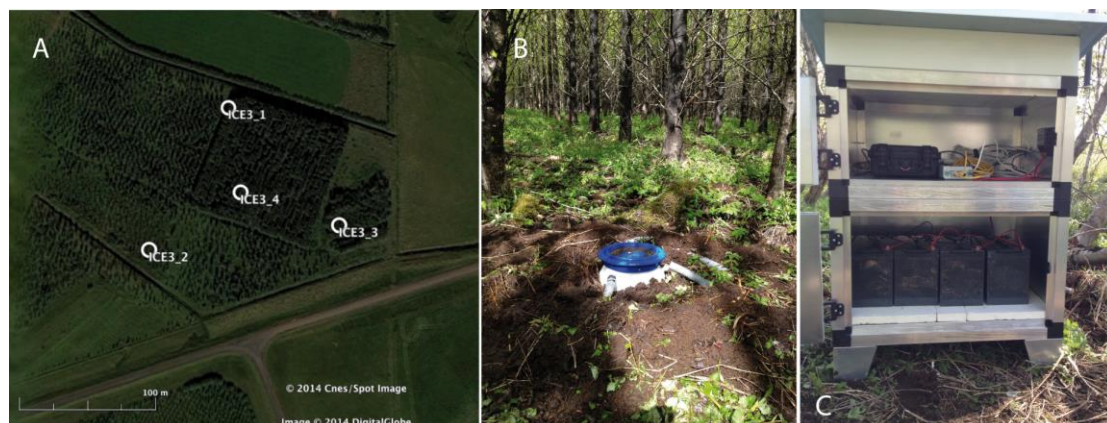


Figure 35: GoogleEarth view of the position of the elements of the ICE2 array and picture of the hut installed at the central element of the array and pole of solar panel in the back.

### 3.1.3. ICE 3 Array

Operating since May 2014, the ICE 3 array is installed in Kirkjubæjarklaustur (Figure 36), at a distance of  $\sim 75$  km to Grimsvotn to the north and  $\sim 55$  km from Katla to the west. The array is equipped with 4 differential pressure transducers (0.001-100 Hz, with  $\pm 100$  Pa dynamic range) and a Guralp CMG/DM24 digitiser. Connection among the elements of the array is obtained with copper cable. GPS time stamped data are both recorded locally on a 16 GByte removable USB memory stick and transmitted with a UMTS/3G modem. Data is recorded in Iceland at the IMO and forwarded to the University of Firenze, in Italy, for real time processing.



*Figure 36: Sensor installation case in the forest, aluminium hut for installation of batteries (lower level) and electronics (upper level) and GoogleEarth view of array elements position.*

### 3.2. Real-time infrasound array Processing

The algorithm for the infrasonic array signal processing is based on the assumption that a signal is coherent at different sensors, while noise does not show any correlation. For the infrasound arrays deployed in Iceland in the framework of the FUTUREVOLC project we have developed a multi-channel correlation algorithm to discriminate signals from noise in terms of wave propagation back-azimuth, apparent velocity and time residual.

- i) The propagation back-azimuth indicates the direction where the signal is coming from and relates to the position of the source respect to the array.
- ii) The apparent velocity is the velocity the wave would have if it was traveling in the same plane as defined by the array.
- iii) Apparent velocity is always higher than real velocity and it relates to the incident angle and thus provides information on the source elevation.
- iv) The time residual is a parameter reflecting the degree of correlation of signal in the array and is the proper detector of signal from noise.

The algorithm to locate infrasound sources has been written in Matlab with graphical interface and it is processing the signals recorded by the three arrays in near real-time. The software is running on-line at the University of Florence (Italy) since March 2014 and at IMO (Iceland) after the end of August and displayed on a web-page (<http://lgs.geo.unifi.it/iceland/ice3.php>; Figure 37). The multi-channel correlation analysis is applied in near-real time to the infrasound array data that are recorded at the UNIFI and IMO, with a maximum delay between the time of recording of an event at the array and processing time of  $\sim 1$  minutes. Multichannel correlation analysis is performed on 5-second-long sliding windows of 0.5-5 Hz band-pass filtered infrasound data from the three arrays. Every time signal is identified from the array, the detection is delivered automatically and in real-time on the dedicated web-page in terms of amplitude at the array, back-azimuth and apparent velocity.

The dedicated webpage (Figure 37) of array processing results is showing the last minutes of band-pass filtered infrasound data recorded by the four element of the array, the 5-second-long time window of analysis (blue square), a map of Iceland centred on the array and showing an arrow indicating the infrasound back-azimuth of infrasound detection. Moreover, processing results of the previous 48 hours are displayed in the webpage, in terms of excess pressure at the array, coherence and infrasound back-azimuth, providing a quick look to the operator of on-going infrasound activity. An interactive map of Iceland allows the operator to switch from one array to the other.

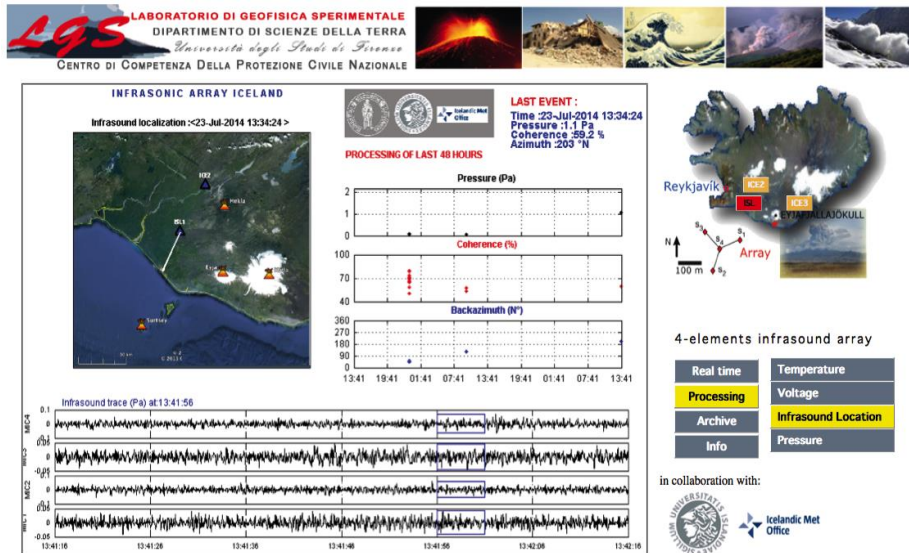


Figure 37: Snapshot of the real-time processing of ICE1 array, as displayed at the IMO and UNIFI. The snapshot refer to real-time data for July 23<sup>rd</sup>, at 13:41:56 UTC, but results for the last 48 hours processing clearly shows the detected events (shaded area).

It is assumed here that the infrasonic wave propagates with a planar wavefront and with a constant velocity across the array. In the case of the array already installed in Iceland the aperture of ~150 m, for frequencies >1 Hz (typical of volcano acoustic signals), it is reasonable to assume the plane wavefront for sources located farther than 700 m from the array.

On July 21, one of the array has successfully detected from a distance of 213 km the infrasound generated by the large landslide occurred at 23:27 at Askja volcano. The detection was delivered automatically and in real-time on the dedicated web-page (Figure 37). Details of the event are provided in the following section.

### 3.3. Results from the FUTUREVOLC Infrasound array network

Below we provide a brief description of two different events, the landslide on Askja volcano and the Bardabunga seismic sequence, to highlight the operation and functionality of the FUTUREVOLC infrasound arrays.

#### 3.3.1. The Bardabunga Seismic sequence

Earthquakes are efficient sources of infrasound, mostly produced by the coupling of the ground shaking to the atmosphere. However, pressure sensors are also sensitive to ground-shaking and careful analysis of array parameters is required to avoid confusion and errors. Here we show signal recorded at all the 3 arrays related to a M5 earthquake from Bardabunga that occurred on August 24th, at 00:09 UTC (Figure 38).

All sensors of the 3 infrasound arrays detected the event at a source-to-receiver distance spanning from a minimum of 90 km (for ICE3 array) up to a maximum of 155 km (for ICE1 array). Real time infrasound processing, described in the previous section did not provide any detection of the signal, because of the high wave propagation velocity across each single array, that was observed to exceed 2000 m/s. Here infrasound arrays are not recording the infrasound produced by the earthquake, at the epicentre or as secondary sources, while they measure the

pressure variation by the vertical ground-shaking of the earthquake at the array. Figure 38 shows the earthquake as recorded by the different elements of the three arrays (ICE1-ICE3) with onset time consistent with seismic wave radiated by the epicentre, and travel times estimated with the different arrays both of volume (6000 m/s) and surface (2000 m/s) waves. This is used to check functionality of the system.

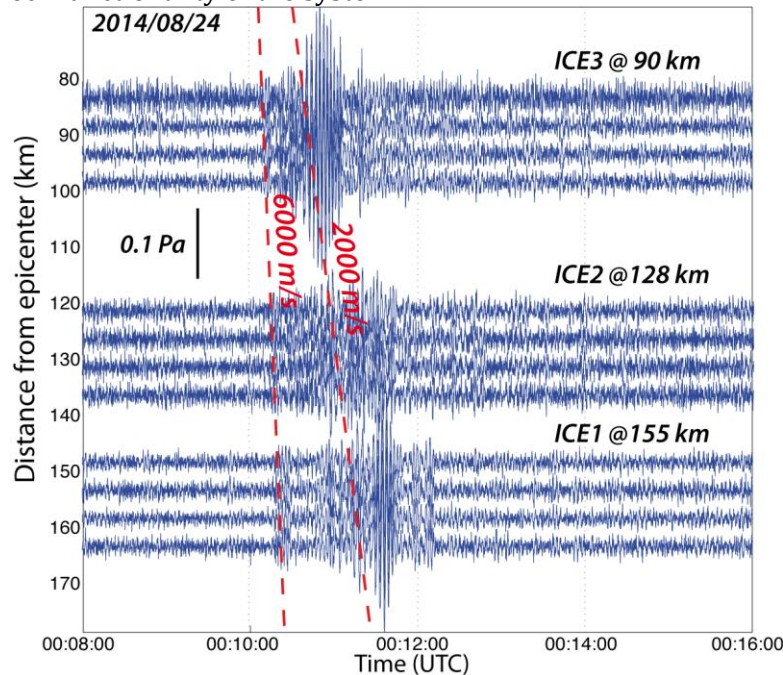


Figure 38: Record of the 00:09 UTC August 24<sup>th</sup>, 2014, M5 Bardabunga earthquake from the different elements of ICE1-ICE3 arrays. Distance among elements of a single arrays is magnified for figure clarity.

### 3.3.2. Landslide at Askja volcano

On July 21<sup>st</sup>, a giant landslide occurred at Askja volcano, with an estimated volume of 50 million m<sup>3</sup> of rock entering the Askja crater lake and producing a tsunami. Preliminary field observations indicate a rotational slide that interested a part of the SE rim of the caldera 700m-wide and 200m-thick that fell down for 340 m. Initial observations suggest waves as high as 40-50 m. A plume was observed above Askja around 23:27 UTC. The event was clearly recorded seismically on broadband stations in Iceland.

A clear infrasonic signal was recorded by ICE 1 array, deployed in Gunnarsholt, at a source-to-receiver distance of 210 km. The signal was detected with the automatic array processing at IMO and UNIFI and result was available online (Figure 37). As described in the previous section, real time data is processed of 5-second-long time windows, looking for coherent infrasound across the array as a function of azimuth and propagation velocity.

The signal, emergent and with a duration of ~ 2 minutes, was recorded with onset time of 22:36:40 UTC. Array processing identifies wave parameters consistent with an infrasonic stratospheric arrival (apparent velocity of 350 m/s) and stable back-azimuth of ~50° pointing directly to Askja volcano. A peak pressure of 0.1 Pa was recorded and amplitude modulation for the whole duration of the signal, as typically observed for stratospheric arrivals is clearly visible.

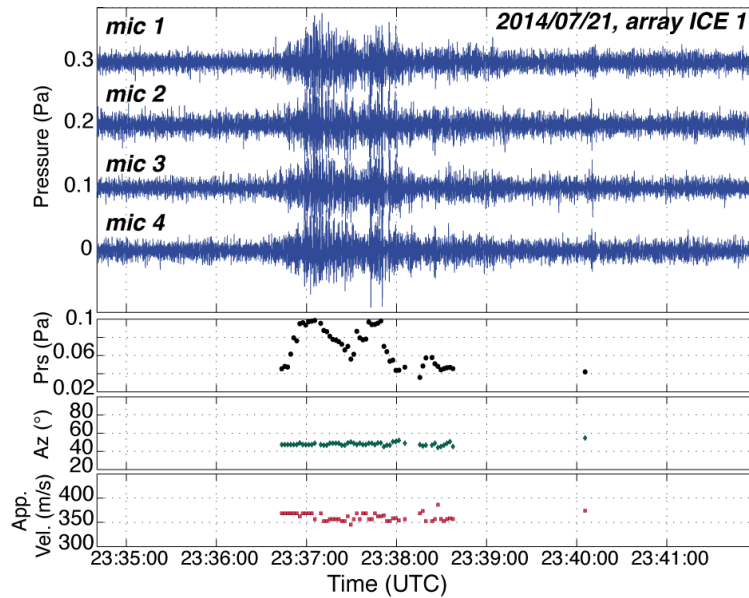


Figure 39: Infrasonic record of the July, 21<sup>st</sup>, 2014, landslide from Askja volcano at ICE1 array, showing signals from the four array elements (0.5-5 Hz band pass filtered) and corresponding wave parameters (pressure amplitude, back-azimuth, apparent velocity) derived from array analysis.

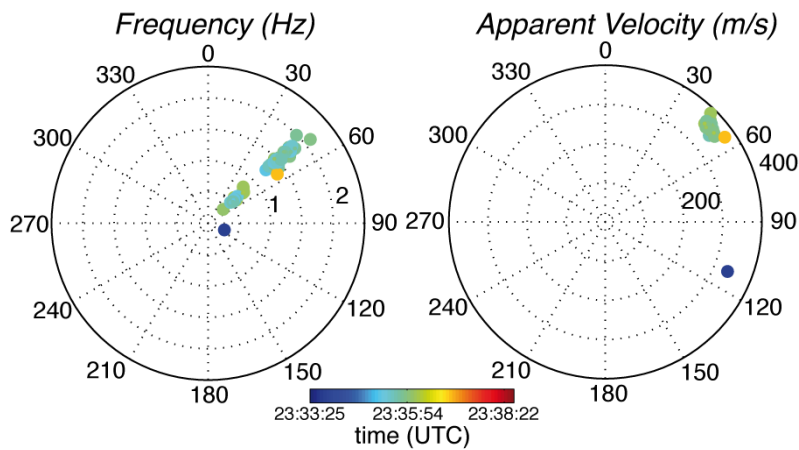


Figure 40: Rose diagram of infrasound detection for the Askja landslide at ICE1 array showing frequency (peaking between 0.5 and 2 Hz) and apparent velocity (stable around 350 m/s). Detections are color-coded as a function of time with detections between 23:36:40 and 23:38:30 UTC.

No signal was observed on the other arrays (Figure 41), deployed at shorter source-to-receiver distances. This is however quite well known, as stratospheric arrivals result from ray-paths ducted in the stratospheric waveguide and produce shadow zones typically 100-200 km wide downwind.

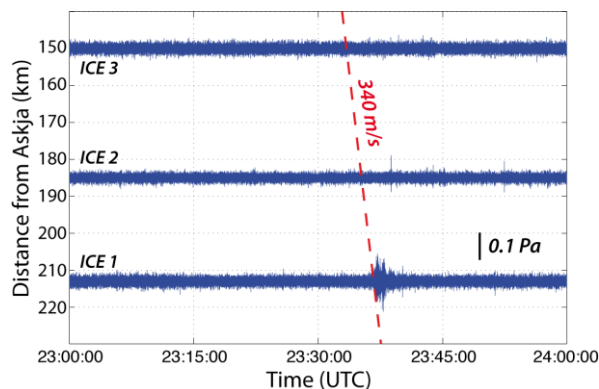


Figure 41: Infrasonic record at the different infrasound array, with travel time for a sound wave marking the arrival at the different source-to-receiver distances. Despite being closer, the other infrasound arrays do not show any record of the Askja landslide.

## 4. Algorithm for stereoscopic viewing field of 3D particle trajectories

This deliverable describes a novel and innovative video monitoring tool that is developed and tested in the frame of FUTUREVOLC. Visual observations of volcanoes provide amongst the strongest and most widely used information of eruption occurrence, plume height or other unrest changes. By use of fixed streaming and time lapse camera installation, this data source shall be analysed using computer vision approaches.

The deliverable aims to test and apply algorithms for determining a three dimensional particle trajectory. The new eruption at Bardarbunga volcano in 2014 provided the unique opportunity to set up cameras, test transportable cameras, and perform image processing as anticipated.

At Bardarbunga (Holuhraun) we recorded videos with several synchronized cameras from 31st August to 4th September 2014. We set the cameras to a high spatial resolution of 1920x1080 and found that a framerate of 25-50 frames/s was sufficient to fully describe the velocity field. The continuous eruption allowed us to set up the cameras in different configurations, monitoring the entire fissure (1, 2, 4 September), or focus on localized parts that were most dynamic (3 September) and where an overlap of the field of view (FOV) of the different cameras was achieved. The ongoing eruption therefore provided the unique possibility to test and improve camera set-up that is important for algorithm testing.

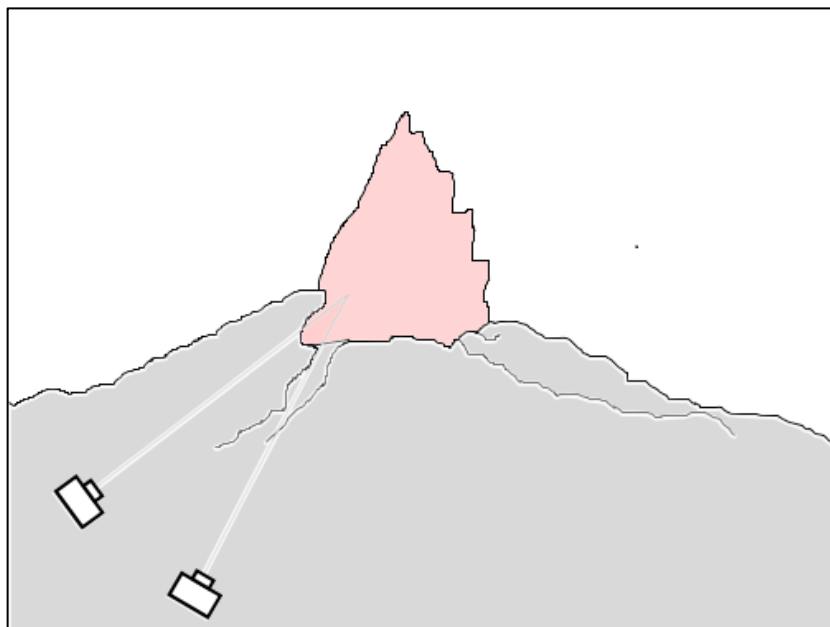


Figure 42: Eruption vents and their lava fountains were recorded from cameras, in order to obtain a two dimensional (2D) and a three dimensional (3D) trajectory dataset. The 3D dataset is derived from video analysis of two or more cameras with field of views (FOV) that are partially overlapping. The figure shows an eruption vent recorded from two cameras.

Velocity fields we calculated from images by computer vision algorithms. There Digital Image Correlation (DIC) and Particle Image Velocimetry (PIV) are the two main image-based methods we tested for displacement measurement.

DIC uses the mathematical correlation functions to analyze digital images of a field undergoing deformation. This technique offers the advantage of obtaining continuous measurements of the whole displacement field. In order to obtain the displacement field, the surface consists ideally of a random 'sprayed-on' speckle pattern. Assuming only one camera is available, the correlation between the deformed images and the undeformed reference image allows to obtain a 2D displacement field that was elaborated in the first project year already (see earlier report). Deformation calculation, based on a Least Squares Matching (LSM) algorithm apply an optical flow approach. That means the deformation is calculated by an affine transformation of sub-areas. The algorithm is iterative. The subpixels are interpolated by bilinear or spline 6-interpolation. Deformation requires an intensity interpolation using existing discrete pixel intensity.

PIV is a method originally developed in the field of fluid dynamics. The displacement vector of each patch during the intervals between two contiguous images is found by locating the peak of the autocorrelation function of each patch. The peak in the autocorrelation function indicates that the two images of each seeding particle overlying each other, so the correlation offset is equal to the displacement vector. For the Particle Image Velocimetry (PIV) different approaches can be used. The general correlation approach calculates the correlation between 2 images, img1 and img2, as:

$$C_{corr}(dx, dy) = \frac{\sum_{i=1}^N \sum_{j=1}^N [f_1(x_i, y_j) - \bar{f}_1][f_2(x_i+dx, y_j+dy) - \bar{f}_2]}{\sqrt{\sum_{i=1}^N \sum_{j=1}^N [f_1(x_i, y_j) - \bar{f}_1]^2} \sqrt{\sum_{i=1}^N \sum_{j=1}^N [f_2(x_i+dx, y_j+dy) - \bar{f}_2]^2}}$$

where f1 and f2 are the small windows from each image in the image pair, N is the window size and the overbar denotes mean quantities. The location of the maximum value in C is used as the

mean particle displacement of this small area. The calculated displacement is retained as 'valid' only if the ratio of the value of the highest peak to the highest peak to the second highest peak exceeds a present threshold value, and the ratio of the values of the highest peak to the r.m.s. (root-mean-square) noise also has to exceed a specific threshold value. The Minimum Quadric Differences (MQD) algorithm is to simply calculate the pixel value differences between the search windows. Thereby the location of the minimum is used as the particle displacement

$$C_{MQD}(dx, dy) = \sqrt{\sum_{i=1}^N \sum_{j=1}^N [f_1(x_i, y_j) - f_2(x_i + dx, y_j + dy)]^2}$$

The MQD is more stable than the normal digital correlation calculation DIC, but is more time-consuming. The 'real' peak of the correlation is calculated by a three-point curve fitting technique that is based on the Gaussian function.

From the combination of several 2D fields of views a 3D particle trajectory is then computed. Each point (x,y,z) of the real coordinates is mapped to the camera coordinate system (x1, x2) for camera 1 and (x2,y2) on images of camera 2. By doing a calibration the mapping function can be calculated and the information of both cameras can be combined. In particular the same point (x,y) is found at different places (x1,y1)/(x2,y2) for different z. This process is reversible: If the points (x1, y1) and (x2, y2) on camera image 1 and 2 are known to belong to the same sample surface position, then using the mapping functions the point (x, y, z) can be determined. To calculate the 3D particle trajectories, the corresponding points (x1, y1) and (x2, y2) in the camera images 1 and 2 by a correlation process to identify the same pattern inside both images. This is done on all points on a grid across the image to reconstruct the surface height in the 'real' coordinates z(x,y).

For Bardarbunga we use all of this information and calculated the surface height changes and displacements over time. The camera position and hence the angle between the cameras and the target fissure is known and the intersection of both camera image planes are in the center of both images, so that the velocities are calculated by:

$$\begin{aligned} x &= x_1 \\ y &= \sin(a) \cdot dx + \frac{\cos(a) \cdot dx - dx}{\tan(a)} \text{ mit } dx = x_2 - x_1 \\ z &= z_1 = z_2 = \text{mean}(z_1; z_2) \end{aligned}$$

where  $x_1$  and  $x_2$  are the values of the vector in the images 1 resp. 2. We define the x-axis of the 'real' coordinate system as the x-axis of the first image. The z-axis is defined as the height. The image below show the marked reference points found. These points have to be the same points in all cameras. Based on the spatial information of all points, the distortion of the images of each camera can be calculated. Furthermore the fit mapping function gives us the coordinates of the image pixels in the 'real' world. Afterwards the calculation we can evaluate our corrected images.

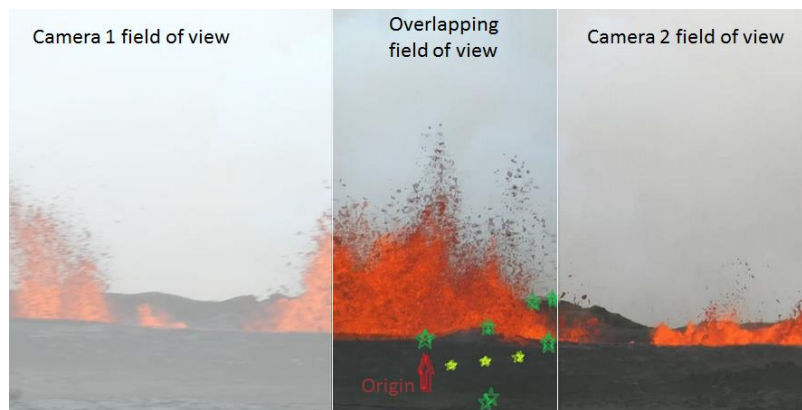


Figure 43: Field of views (FOV) from two cameras, 2014 Bardarbunga eruption. Three dimensional displacement fields are calculated within the overlapping FOV, using the algorithm described above. Green stars mark reference points selected in both images.

Therefore, the task of the FUTUREVOLC project could nicely show the technical realization of an innovative approach to set up cameras and computer vision algorithms to determine the 3D velocity field and possible changes occurring in the vent region, implemented and tested for the 2014 Bardarbunga eruption. We found nevertheless, that due to the computational effort, a two dimensional velocity reconstruction is particularly well suited for volcano monitoring programs, because of the near real time computation and trajectory estimation possibilities.

## 5. References

- Bonadonna C, Volentik A., Smith K.T., Costa A., Connor C.B., (2009) *Behind A Database: The Characterization of Explosive Eruptions*, American Geophysical Union (San Francisco, USA, 14-18 December 2009).
- Johnson, J.B., M. Ripepe (2011), *Volcano Infrasound: A review*, *J. Volcanol. Geoth. Res.*, 206, 61-69, doi:10.1016/j.jvolgeore.2011.06.006.
- Matoza, R. S., J. Vergoz, A. Le Pichon, L. Ceranna, D. N. Green, L. G. Evers, M. Ripepe, P. Campus, L. Liszka, T. Kvaerna, E. Kjartansson, Á. Höskuldsson (2011), *Long-range acoustic observations of the Eyjafjallajökull eruption, Iceland, April–May 2010*, *Geophys. Res. Lett.*, 38, L06308, doi:10.1029/2011GL047019
- Ripepe, M., C. Bonadonna, A. Folch, D. Delle Donne, G. Lacanna, E. Marchetti and A. Höskuldsson (2013), *Ash-Plume Dynamics and Eruption Source Parameters by infrasound and thermal Imagery: the 2010 Eyjafjallajökull Eruption*, *Earth Planet. Sc. Lett.*, 366, 112-121, doi:10.1017/j.epsl.2013.02.005.
- M. Ripepe, E. Marchetti (2002), *Array tracking of infrasonic sources at Stromboli volcano*, *Geophys. Res. Lett.*, 29, 2076, doi:10.1029/2002GL015452.
- Vergnolle, S., G. Brandeis (1994), *Origin of the sound generated by Strombolian explosions*, *Geophys. Res. Lett.*, 21(18), doi: 10.1029/94GL01286.

*Walter TR (2011) Structural architecture of the 1980 Mount St. Helens collapse: an analysis of the Rosenquist photo sequence using digital image correlation. Geology, v. 39 (8), 767-770, doi: 10.1130/G32198.1.*